Direct evidence for a nonzero energy gap and half-metallicity in the diamondlike ferromagnet (Zn,Mn) Ge P 2

Article · August 2024

DOI: 10.1103/PhysRevB.110.064406

3 authors:

Gennady A. Medvedkin
GM Glass
101 PUBLICATIONS **1,121** CITATIONS
SEE PROFILE

Katsuaki Sato
Tokyo University of Agriculture and Technology
292 PUBLICATIONS **3,939** CITATIONS
SEE PROFILE

Takayuki Ishibashi
Nagaoka University of Technology
201 PUBLICATIONS **2,019** CITATIONS
SEE PROFILE

Direct evidence for a nonzero energy gap and half-metallicity in the diamondlike ferromagnet (Zn,Mn)GeP$_2$

Gennady Medvedkin,[1,*] Katsuaki Sato,[2] and Takayuki Ishibashi[3]
[1]*General Molded Glass, Inc., Torrance, California 90502, USA*
[2]*Tokyo University of Agriculture and Technology, Tokyo 184-8588, Japan*
[3]*Nagaoka University of Technology, Nagaoka, Niigata 940-2188, Japan*

(Received 10 November 2023; revised 21 June 2024; accepted 19 July 2024; published 7 August 2024)

A giant narrowing of the energy gap in the nonlinear optical crystal ZnGeP$_2$ (ZGP) after the incorporation of manganese atoms into the chalcopyrite crystal lattice has been detected. The (Zn,Mn)GeP$_2$ (ZMGP) thin films grown by solid-phase endotaxy on ZGP (001) substrate share the tetrahedrally coordinated structure of chalcopyrite. The measured fine crystal structure and fundamental optical properties point to a semiconductor substance. However, other properties, such as electrical conductivity, current transport across the energy barrier ZMGP/ZGP, and photoemission of holes from the ferromagnetic ZMGP layer, claim that this substance is a metal. We investigated this unusual combination of properties in ZMGP using comprehensive measurements, including detailed chemical composition at the surface and in depth, and obtained direct experimental evidence for half-metallicity (HM) in the Mn-rich ZMGP material. Existing theories agree with these experimental proofs obtained. We discuss possible emitters of spin-polarized holes on these HM films operating at room temperature in fully diamondlike structures.

DOI: 10.1103/PhysRevB.110.064406

I. INTRODUCTION

The ZnGeP$_2$ (ZGP) crystals belong to energy materials that play a central role in nonlinear optical energy conversion technologies. Undoped ZGP crystals are used in laser-based nonlinear optical devices that convert enormous energy in the midinfrared (mid-IR) spectral range [1–9]. When doped with appropriate 3*d* magnetic ions, ZGP crystals turn from diamagnetic to ferromagnetic (FM). In FM-based devices, electron spins as information bits can be used with extremely low-energy consumption for up-and-down flips. Utilization of spins for magneto-optical control can occur energetically efficient and fast. The energy difference in these two simultaneous high- and low-energy applications of Mn-doped ZGP crystals can be as high as 10^{20} times. Controlling the powerful light flux using low-energy magnetism and spin injection into crystals may open an unusual path in the field of nonlinear optics.

Since the discovery of the class of FM chalcopyrites II-IV-V$_2$ with Curie temperatures above room temperature (RT) [10–17], more than 1000 publications have been issued on this topic. Theoretical developments of FM chalcopyrites have extended the family of ternary compounds with spin-dependent properties [18,19]. Several theoretical models explain FM at RT [20–25], while earlier simple models contradictorily indicated antiferromagnetic (AFM) ordering [26,27]. The half-metallic (HM) state in (Zn,Mn)GeP$_2$ (ZMGP) was theoretically found in Refs. [21,25,28–30]. However, experimental data exhaustively describing the HM properties of this solid are not available. Hole transport in a magnetic field [31], magnetization and magneto-optics [32–34], and magnetic resonances [35–38] in low-doped ZnGeP$_2$:Mn (ZGP:Mn) and Mn-rich ZMGP materials describe magnetically dependent properties. *In situ* ultraviolet photoemission spectroscopy (UPS) and x-ray photoemission spectroscopy (XPS) measurements [39] showed the transition from metallic to semiconductor (SC) type in a ZMGP/ZGP structure. These experimental results have only characterized the SC properties or the metallic Fermi edge at the surface, but no direct evidence for HM in ZMGP has been published to date. In this paper, we provide a multiexperimental proof of the HM behavior of Mn-rich ZMGP, including its SC and simultaneously metal properties in the same substance. These properties encompass the fundamental optical absorption and reflection, crystal structure, temperature dependence of resistivity, electric current transport, and internal photoemission (IPE) in a ZMGP/ZGP heterostructure operating as a Schottky diode. We did not focus on the measurements of the percent spin polarization because, on the one hand, it is an established fact that the HM is a fully spin-polarized material, and on the other hand, there are still many controversies in measuring the correct value of spin polarization [40,41]. Moreover, HMs are not the only class of solids where 100% spin polarization can be realized: recently emerged spin-gapless SCs (SGSs) have demonstrated full polarization for electrons and holes at the Fermi level [42–47]. Theory predicts a zero band gap in SGSs, so optical spectra, hole photoemission, and hole transport experiments can directly discriminate which class of solids the substance under study belongs to.

Overall, we present a comprehensive study of optics, photoelectronics, crystal structure, electric current transport, and

---

[*] Contact author: g_medvedkin@yahoo.com

resistivity based on reliable and well-established techniques, which we believe provides direct experimental evidence for HM in Mn-rich ZMGP.

To further explore the crystal structure, we first present details of the growth method called endotaxy, Auger spectroscopy, and precision x-ray analysis of ZMGP layers grown on the ZGP crystal. We then present a crystal model of the tetrahedron and discuss magnetic chains and nanoclusters. Finally, we describe in detail the fundamental optical absorption, reflection, electrical resistivity of ZMGP, current transport, and photoemission of holes in the ZMGP/ZGP diode structure.

The FM chalcopyrites, such as ZMGP and 100% substituted $MnGeP_2$, were already grown using both endotaxial and epitaxial methods [13,48–54]. At high [Mn] concentration, these materials exhibit FM at RT, and furthermore, FM persists at lower [Mn] concentrations ($x < 5\%$) in the diluted magnetic SC (DMS) phase, as shown for the precise layer-by-layer removal of ZMGP from the surface of a ZGP crystal [39]. The theory performed for $Cd_{1-x}Mn_xGeP_2$ confirms the isolated Mn_{Ge} defect to generate a shallow acceptor level, which is strongly spin polarized [20]. The spin states are split such that the up-spin level is higher and the down-spin level is lower than the valence band maximum (VBM) [20]. Significant valence band spin splittings and spin polarization were found in five Mn-doped chalcopyrites, including $Zn_{1-x}Mn_xGeP_2$ ($x = 6\%$) [28]. This feature creates a paradigm for nonlinear optical crystals such as ZGP due to their robust diamondlike crystal structure and spin polarization.

Then spin-polarized electrons must be injected or emitted into another nonmagnetic material structurally matched. Mn-doped II-IV-V_2 chalcopyrites among a variety of diamondlike materials (IV, III-V, II-VI, and I-III-VI_2) are the most promising in terms of realizing RTFM as injector layers on other well-developed Si or GaAs SCs. They are compatible with various diamondlike materials such as Si, Ge, GaAs, and GaP due to their tetrahedral coordination and close lattice constants, which allow the growth of almost perfect heterojunctions [48–54]. The lattice constants of Mn-doped ZMGP layers are also close to those of ZGP crystal [13,14,34].

Mn-dopant and native point defects in $ZnGeP_2$ play an important role in the realization of RTFM. The modeling of point defects in ZGP crystals has been extensively studied in Refs. [55–59]. Various theoretical models for heavily Mn-doped $ZnGeP_2$ suggested the HM [18–22,25,28–30] or, controversially, a normal FM metallicity [60]. According to Ref. [18], HM persists for $ZnGeP_2$ including another 18 hosts II-IV-V_2 at higher Mn concentration (50%). Even if Mn completely occupies the group-IV element site, the resulting stoichiometric compounds are HMs in all cases except for the nitrides [18,28–30]. Despite many theoretical papers and books on spintronics [61–69], the hot topic remains for the choice of the right material with significant spin splitting, spin polarization, and structural and chemical compatibility with Si, Ge, III-V, and II-VI in the frame of the diamondlike crystal structure operating at RT with $T_C > 300$ K. Thus, the experimental detection of all bound properties corresponding to the HM state in this material is important.

II. EXPERIMENT

A. Sample preparation and measurements

$ZnGeP_2$ single crystals grown by the vertical Bridgman method were cut from a crystal ingot in the isotropic direction with a base plane of (001). Crystal plates were mechanically polished, finished, and etched in a Br-methanol solution for a few tens of seconds. FM endotaxial layers were grown in the molecular beam epitaxy (MBE) chamber using the solid-phase chemical technique. Auger electron spectra (AES) were recorded using an Omicron Nano Technology instrument in the MBE machine with primary electron energy of 3 keV, a lock-in amplifier, and 1 eV peak-to-peak energy modulation. AES in the differential mode were taken at electron kinetic energies from 40 to 1200 eV.

X-ray diffraction (XRD) reflectivity curves were taken on a Rigaku type RAD-IIC x-ray diffractometer in the $\theta/2\theta$ scan for the Bragg-Brentano geometry. The detail structure of heterojunctions was characterized by high-resolution XRD (HRXRD) patterns taken in a coupled $\omega/2\theta$ scan (Cu $K\alpha_1$ radiation, $\lambda = 1.5406$ Å) employing two diffractometers: a PAnalitical X'pert and a Rigaku type RINT-RAPID system with a glancing angle incidence. The HRXRD system was equipped with a four-axis goniometer.

After growing the magnetic ZMGP layer, the heterojunction samples were refreshed with the same etching solution just before measurements. The optical study was carried out with grating and Fourier transform IR (FTIR) spectrophotometers, a Perkin-Elmer lambda 950, equipped with PMT and PbS detectors, and a Shimadzu FTIR-8400s equipped with KBr optics. For optical reflection spectra, a small kink at the energy 1.38 eV (900 nm) was because of switching the photodetector in the spectrophotometer. The Kramers-Kronig transform was applied to extract the absorption components from the complex reflection spectrum in the deep fundamental band 0.5–6.0 eV.

Electrical resistivity was measured by a four-probe method using the vacuum deposited Au-dot contacts. Measurements were conducted in the temperature range 4.2–350 K. Current-voltage (I-V) characteristics and spectral photoresponse at photon energies of 0.8–3.8 eV were measured at 300 K. The Fowler hole emission in the Schottky barrier was recorded at RT.

B. Endotaxy of (Zn,Mn)GeP_2

Successful endotaxial growth by solid-phase reactions is known in simple chemical systems, e.g., Ge-Mn [70]. The hexagonal structure of the Mn_5Ge_3 layer grown on the Ge (111) substrate with a diamond crystal structure has, however, obvious crystallographic limitations because of different syngonies. Another system $CdGeP_2$-Mn with a ternary diamondlike compound is more compatible crystallographically. It was successfully used in a solid-phase reaction to grow a RTFM endotaxial layer of (Cd,Mn)GeP_2 (CMGP) sharing the crystal structure of chalcopyrite $I\bar{4}2d$ [14,15,34]. Similar endotaxial processing was applied to $ZnGeP_2$ crystals in this paper.

One of the most efficient nonlinear optical crystals $ZnGeP_2$ is the material of choice for several applications in mid-IR lasers, and growing a ZMGP solid solution on top of the crystal offers additional advantages in magneto-optical control of high-power mid-IR laser sources. The endotaxial approach brings the lattice constants of the materials closer to each other and avoids deformation at the heterointerface with excellent single crystallinity over a wide range of Mn concentrations. The crystallographic orientation of the layers strictly repeats the (001) orientation of the substrate, following the structural correspondence condition by definition. The solubility (substitution) of Mn in the ZGP lattice is full, and the lattice constants of ZGP and MGP compounds limit the range of the lattice constant variation a and c (if Vegard's law is valid for the ZMGP solid solution). At least, it is known that the crystal structure of $ZnGeP_2$ and $MnGeP_2$ is chalcopyrite, and $a/c = 5.466/10.722$ Å for ZGP [34], $a/c = 5.693/11.303$ Å for MGP epilayers [47–49], and $a/c = 5.655/11.269$ Å for bulk MGP powder [24], respectively. The lattice mismatch in the virtual heterojunction of these ternary compounds is $\delta a = 2\Delta a/\Sigma a = 3.4 - 4.1\%$, and $\delta c = 2\Delta c/\Sigma c = 5.0 - 5.3\%$. According to Vegard's law, the $Zn_{1-x}Mn_xGeP_2$ solid solution with $0 < x < 1$ should have constants right between ZGP and MGP within the same crystal structure of chalcopyrite, and the mismatch with the ZGP substrate is expected to be smaller.

Endotaxy in the MBE chamber comprises two steps: (1) deposition of a thin layer of Mn metal on the $ZnGeP_2$ face and (2) thermal diffusion of manganese atoms inward during simultaneously substituting Zn and Ge for Mn in the two cationic sublattices of the host crystal. The temperature of the solid-phase reaction was chosen much lower than $T_{\mathrm{dec}} = 973$ K, the decomposition temperature of $ZnGeP_2$ [71], and based on thermal chemical stability of the ternary compound as $\frac{1}{2}\, T_{\alpha-\beta} \pm 75$ K, where $T_{\alpha-\beta} = 950$ K is the solid state α-β transformation temperature [72]. We employed an initial 50-nm-thick Mn metal layer, like $d = 51$ nm in Ref. [39].

ZMGP layers were grown endotaxially using different deposition and diffusion temperatures: (1) $T_{\mathrm{dep}} = T_{\mathrm{dif}} = 400\,^{\circ}\mathrm{C}$, (2) $T_{\mathrm{dep}} = 20\,^{\circ}\mathrm{C}$, $T_{\mathrm{dif}} = 550\,^{\circ}\mathrm{C}$, and (3) $T_{\mathrm{dep}} = 100\,^{\circ}\mathrm{C}$, $T_{\mathrm{dif}} = 500\,^{\circ}\mathrm{C}$. The depth distribution of Mn in ZMGP/ZGP was evaluated using accurate layer stripping at a sputter etch rate of 2 Å/min by *in situ* UPS and XPS measurements [39]. The formation of Mn-rich and Mn-poor layers in the ZMGP/ZGP heterostructure was detected (Sec. III D). The charge carrier transport in the upper layer of Mn-rich ZMGP revealed their metal-like origin [31,38]. The distribution of manganese in the Cd-analog CMGP/CGP was also observed in the cross-sectional scanning electron microscope (SEM) [10,11] and found a distinct black-and-white contrast in the images between the top layer and the underlying crystalline volume. The layer-substrate profile indicates a strong difference in the electrical conductivity and hence electron density in the film compared with the substrate [34,48].

The buffer interface ZGP:Mn with a low Mn concentration formed in the diffusion-reaction process below the upper Mn-rich ZMGP layer. The low-doped buffer naturally minimizes the lattice mismatch between the two components, and the entire heterojunction retains the diamondlike structure with isotropic orientation [001]. Therefore, the transition from the top layer to the undoped substrate occurs smoothly without lattice stress. Unlike conventional MBE growth from external sources, this growth method consumes the seed material to build up a layer with a lattice orientation replicating that of the substrate. During the solid-phase chemical reaction, the major substitution Mn → Zn is maintained due to the activity series of metals, where manganese is higher in reactivity than zinc, cadmium, or tin, and therefore, Mn vigorously displaces them in II-IV-V_2 compounds. An additional resource that promotes the chemical reaction in the desired direction is the Zn vacancy, and the solid-phase reaction obeys the equation:

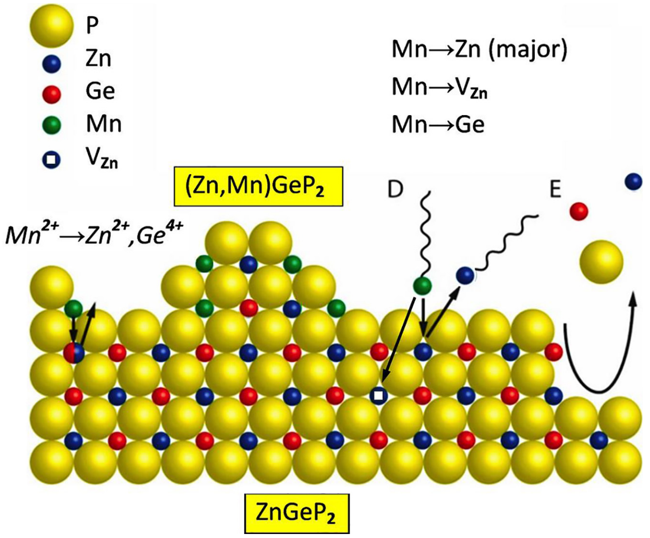

FIG. 1. Atomic mechanism of diffusion-substitution-emission processes on the surface of $ZnGeP_2$ in the solid-phase chemical reaction with Mn.

$$\begin{aligned} ZnGeP_2 + V_{Zn} + Mn &\to (Zn_{1-x}Mn_x)GeP_2 \\ &+ Zn(Mn_yGe_{1-y})P_2 + (MnP)_{\mathrm{nc}} \to \mathrm{ZMGP} + (MnP)_{\mathrm{nc}}, \end{aligned} \tag{1}$$

where $x >> y$ are partial concentrations, $x + y = [\mathrm{Mn}]$ is a full concentration, and nc is a nanocluster.

The molar fractions x, y are principally regulated by the Pauling electronegativity of cations Mn, Zn, and Ge, and nanoclusters nc are dissolved in the lattice matrix. The substitution Mn → Ge proceeds as a minor reaction due to the higher valence and much smaller ionic radius of the Ge^{4+} cation, although a small excess of Ge may be present in the chalcopyrite matrix due to an extended homogeneity range of II-IV-V_2 compounds and can slightly enhance this substitution. This minor substitution Mn_y is responsible for the realization of the RTFM state in ZMGP [Eq. (1)] and confirmed by simulations [20,21]. MnP exists as nanoclusters diffusely distribute in the crystal matrix and remain stealth to x rays in a standard setup (see explanation in Sec. III B).

A visual representation of atomic exchange in the solid-phase chemical reaction is shown in Fig. 1. Diffusion (D) of atoms inward and emission (E) of atoms outward occur under high-vacuum conditions, which ensures efficient substitution of two cations and zinc vacancy for manganese atoms in $ZnGeP_2$. This reaction leads to the endotaxial growth of the Mn-rich ZMGP layer on the surface and low-doped Mn diffusion layer beneath it. While substitutions of the group-II cation and V_{Zn} do not change electronic charge states, the

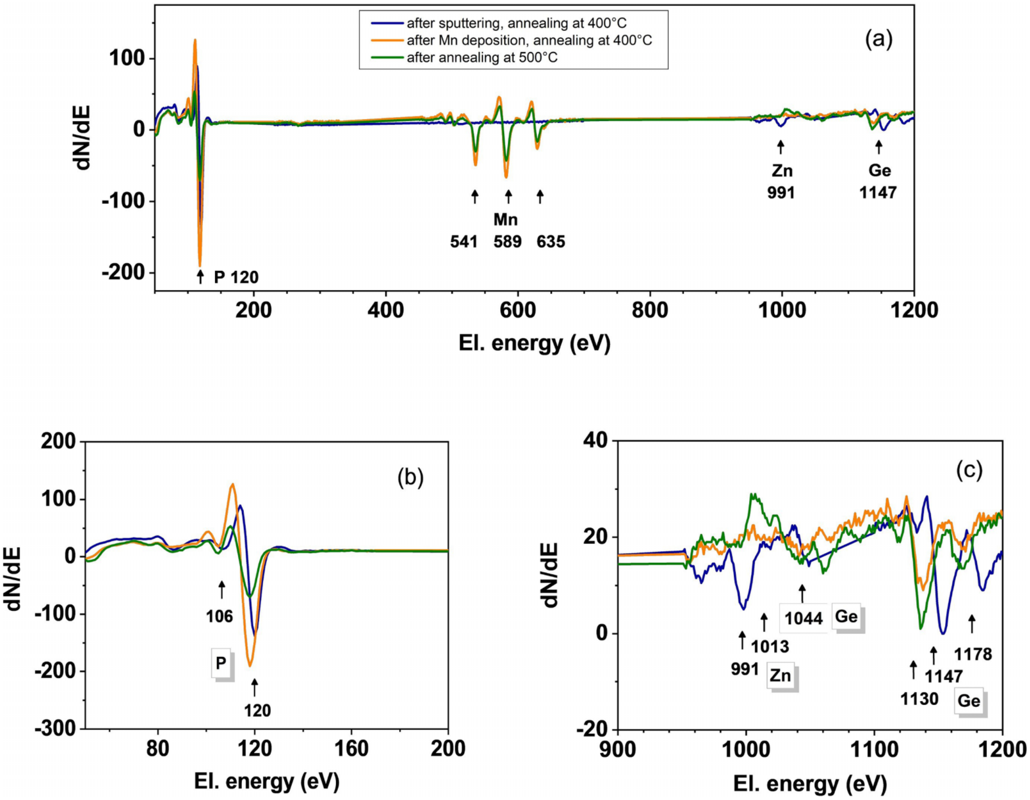

FIG. 2. Auger electron spectra (AES) for the clean ZGP surface and ZMGP layers grown at 400 and 500°C. (a) AES signals for all chemical elements and well-resolved three peaks for Mn; (b) and (c) magnified AES signals for phosphorous, zinc, and germanium.

substitution of Mn → Ge is accompanied by the generation of two extra holes, and the group-IV cationic site acts as a double acceptor. The intercation exchange $\mathrm{Mn_{Ge}} \leftrightarrow \mathrm{Mn_{Zn}}$ is also available at elevated temperatures.

Let us briefly list the advantages and disadvantages of endotaxy for growing ideal thin layers of ZMGP:

Advantages:

(1) A single Knudsen cell (Mn) is used for deposition.

(2) The solid-phase chemical reaction is determined by the electronegativity of the reacting metals.

(3) Cation substitution occurs predominantly at the Zn site and secondarily at the Ge site.

(4) The crystal orientation of the endotaxial layer is set by the host substrate.

(5) The heterojunction has a smooth interface due to a ZGP:Mn buffer layer.

(6) The endotaxial layer is not stressed or stretched and has a relaxed crystal structure.

Disadvantages:

(1) The layer thickness can only be controlled by the metal thickness of Mn and temperature.

(2) Multilayer growth is inconvenient.

(3) The Mn distribution profile is mainly determined by diffusion creating an extended interface.

The listed pros and cons highlight the simplicity, cost effectiveness, and convenience of the Mn-related endotaxy used. While endotaxy allows the growth of ZMGP and CMGP layers with a maximum $x \sim 0.50$ [10,11,23,39], epitaxy has demonstrated the growth of MGP films with $x = 1$ [24,49–51].

III. RESULTS

A. AES

The AES technique was used *in situ* as a surface-sensitive method to characterize the chemical elemental composition in the outer 0.5–5 nm layer. The electron beam excited characteristic emission from the surface, so it is fortunate that the top layer of ZMGP is electrically conductive, and AES analysis can be successfully applied without local charging problems.

The initial crystal surface was cleaned in the MBE chamber by sputtering to remove the carbon and oxygen contaminants. The carbon signal at characteristic kinetic energies of 242 and 273 eV and oxygen signal at energies of 471, 488, and 510 eV [73] is close to the noise level that is typical for clean surfaces of III-V compounds with similar treatment. The upper Mn-rich layer was analyzed for chemical elements P, Mn, Zn, Ge, O, and C, and results are shown in Fig. 2. The dN/dE peaks are well resolved for clean surfaces of the two original $\mathrm{ZnGeP_2}$ crystals and coincide with each other. The AES sensitivities are high, 0.50 and 0.20 for oxygen and carbon, respectively, so these light contaminants were confidently removed by sputtering. On the clean ZGP surface after initial sputtering, AES peaks were observed only for the elements P, Zn, and Ge (blue curves). After Mn deposition and thermal processing, additional signals associated with manganese were recorded, Fig. 2(a), green and orange curves. The Mn-related signals were calibrated using GaMnAs samples with measured dN/dE peaks at 535, 581, and 628 eV. The elements P (0.5), Mn (0.21), Zn (0.18), and Ge (0.10) clearly appear on the surfaces of both ZMGP films grown at $T = 400$ and 500°C.

The full spectrum in Fig. 2(a) well resolves three main peaks belonging to manganese at 541, 589, and 635 eV and weaker peaks at 535 and 509 eV [73]. The intensity of Mn peaks indicates that the diffusion rate of manganese at high temperatures is higher than at low temperatures. Thus, the penetration of Mn into the crystal at $T_{\text{diff}} = 500\,^{\circ}\text{C}$ is higher than at 400°C, and the Mn peak becomes lower due to less [Mn] on the surface. Panels (b) and (c) show the magnified signals for phosphorus, zinc, and germanium with the strongest peaks. Characteristic electron energies are known for P (120 and 106 eV), Zn (991, 1013, 913, 833, and 902 eV), and Ge (1147, 1178, 1030, 1075, 1056, and 963 eV) [73]. Most of the obtained peaks agree with these reference data; the main ones are shown by arrows. The chemical shift for the experimental peaks varies from 0 to 14 eV and is related to the change of the oxidation state of cations after Mn doping. Almost all elements in the periodic table exhibit a chemical shift in approximately the same energy range as in the presented AES spectra. For example, the Auger peaks of the germanium crystal and germanium oxide layer are separated by >8 eV for the two oxidation states Ge^0 and Ge^{4+} [74]. These shifts arise mainly from changes in oxidation final-state effects due to changes in the chemical environment of the atom or variations in relaxation energy due to different electrical conductivities [75,76]. The P peaks at 120 eV in Fig. 2(b) do not overlap with other AES signals, but the Zn and Ge peaks in Fig. 2(c) undergo peak overlap. The amplitude of the main P peak changes after Mn doping, indicating an increase in phosphorus concentration at 400°C and a decrease at 500°C. The main Zn and Ge peaks vary in both intensity and energy shift. Indeed, the electrical conductivities of ZGP and ZMGP differ by many orders of magnitude, see Secs. III J and III K. Identification of Auger peaks is generally easier for light elements than for heavy elements because of the interference of heavy-element peaks with a larger number of transitions. Higher-energy peaks have a larger width [full width at half maximum (FWHM) is typically 3–10 eV], so peak overlap is more likely [76]. Thus, the identification of Zn and Ge peaks is a more difficult task.

During endotaxy, the occupation of Mn_{Zn} sites increases, and the chemical reaction shifts to the right side in Eq. (1). At 400°C, the Zn peak at 991 eV almost disappears, Fig. 2(c), and the substitution by Mn atoms occurs completed near the surface. At the same time, [Ge] changes insignificantly, and the substitution Mn → Ge remains only minor. The situation changes dramatically at 500°C, and the Zn signal reappears with a weaker amplitude, Fig. 2(c). This means that an additional amount of zinc enters the outer layer again, and the balance shifts to the left side of Eq. (1), enriching with [Zn]. The Ge peak at 1147 eV changes slightly in magnitude, but the energy shift associated with the oxidation state is much more pronounced. Some Ge atoms move into the lattice interstitials with changing oxidation state. AES show that, at higher temperatures, Zn atoms move intensively toward the surface and outward, while Mn atoms penetrate deeper. The mutual movement of atoms in and out for zinc and germanium leads to a decrease of the cation ratio [Zn]/[Ge] near the surface, which is consistent with the analysis of binding energies [39].

Given that ternary compounds II-IV-V_2 possess a wide region of homogeneity, a small excess of $(\text{MnP})_{\text{nc}}$ at a level comparable with intrinsic point defects seems very plausible. At higher temperature (500°C), excess Zn atoms escape from the crystal surface and give noticeable AES signals at energies of 980–1030 eV, as shown in Fig. 2(c), green curve. These AES confirm that, during manganese-crystal interaction: (1) the quasichemical reaction, Eq. (1), is reasonable and suitable to explain the mutual movement of atoms; (2) the concentration [Zn] changes mainly, [P] changes slightly, and [Ge] remains almost unchanged; and (3) the oxidation state of some Ge ions changes. Massive substitution occurs in the II-cation sublattice, and minor substitution occurs in the IV-cation sublattice [10,20]. Thus, the reaction of Mn with II-IV-V_2 compound proceeds according to the rule: *Massive substitution occurs at one cation site, and minor doping occurs at the other cation site.*

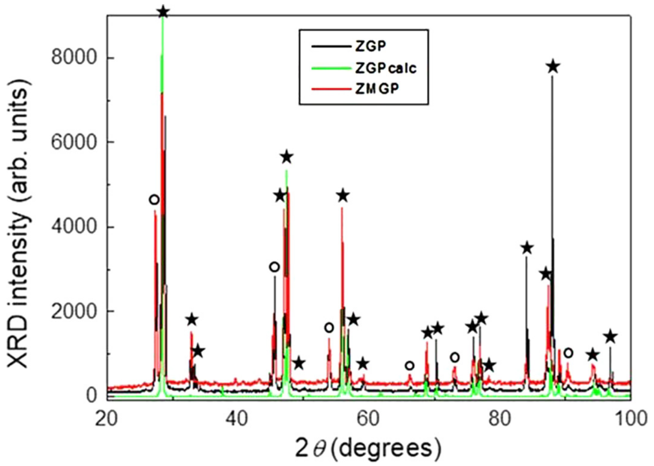

FIG. 3. X-ray diffraction (XRD) patterns of $\text{Zn}_{1-x}\text{Mn}_x\text{GeP}_2$ powders with [Mn] = 0 and 20%, and the calculated peaks of pure ZnGeP_2. Stars indicate chalcopyrite; circles indicate the excess germanium.

B. XRD

XRD was studied for bulk materials: polycrystalline ZnGeP_2 and polycrystalline $\text{Zn}_{1-x}\text{Mn}_x\text{GeP}_2$ with $x = 0.2$ (Fig. 3) and for single-crystalline heterojunction ZMGP/ZGP (Fig. 4). The solid solution ZMGP was advisedly synthesized with [Mn] = 20% in the form of a polycrystalline ingot [13,14] and then ground into powder for XRD measurements. The experimental 2θ-scan patterns in Fig. 3 are compared with the XRD curve calculated for the undoped pure ZGP. The measured (black curve) and calculated (green curve) are in good agreement with each other. Homogeneous polycrystalline bulk materials ZMGP (20 and 50% Mn) were also grown in two syntheses [15]. Figure 3 shows only the 20% Mn sample (red curve) for comparison with measured and calculated ones in this paper. ZGP and ZMGP give similar peaks marked with stars and belong to the chalcopyrite crystal structure. The excess Ge in the ZGP ternary compound is known even for high-quality nonlinear optical crystals. XRD lines related to germanium were observed in both undoped and Mn-doped polycrystalline materials.

A detailed examination of the peak position indicates that the main ZMGP diffraction lines are shifted toward

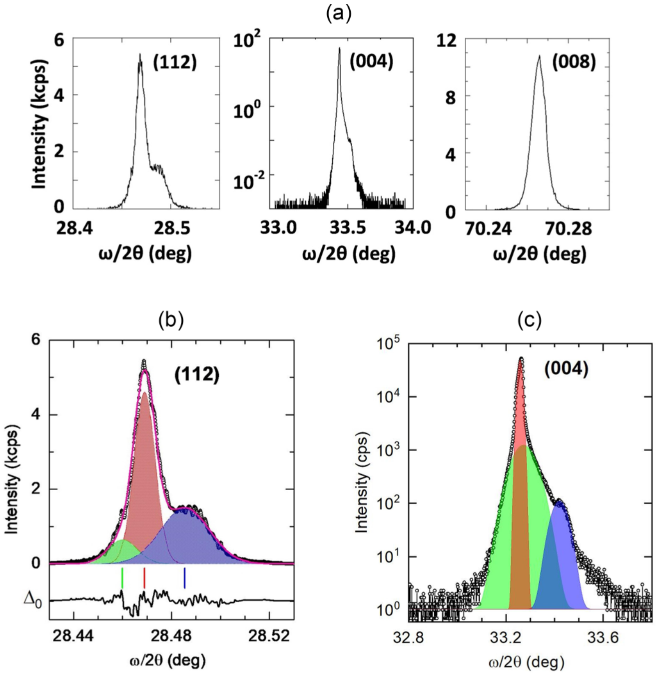

FIG. 4. High-resolution x-ray diffraction (HRXRD) patterns for ZMGP/ZGP heterojunction (a) taken on reflexes (112), (004), and (008). (b) Three peaks deconvolution of the (112) reflex. Δ_0 is a random residual standard deviation and red-green-blue (RGB) bars denote maxima. (c) Three peaks deconvolution of the (004) reflex in semilogarithmic scale.

TABLE I. Attenuation length L of x-ray radiation at $\lambda = 1.5406$ Å in materials. The grazing angles correspond to planes $hkl = (112)$ and (004), ratio = $L_{\mathrm{ZGP}}/L_{\mathrm{film}}$. Denotations for MnP crystal structures: *zb* – cubic (zinc-blende), *hex* – hexagonal, *or* – orthorhombic.

Material	Density (g/cm^3)	L (μm) at ω angle 14.22°	16.71°	Ratio
$\mathrm{ZnGeP_2}$	4.175[a]	9.002	10.537	1.0
[Mn] 8%	4.120[b]	8.504	9.955	1.1
[Mn] 20%	4.039[b]	7.868	9.21	1.1
[Mn] 50%	3.834[b]	6.694	7.836	1.3
[Mn] 80%	3.629[b]	5.901	6.907	1.5
$\mathrm{MnGeP_2}$	3.493[c]	5.506	6.445	1.6
MnP-*zb*	3.93[d]	3.14	3.675	2.9
MnP-*hex*	5.50[d]	2.243	2.626	4.0
MnP-*or*	5.94[d]	2.077	2.431	4.3

[a] Reference [72].
[b] This paper.
[c] Reference [24].
[d] Reference [79].

smaller angles 2θ and give a larger lattice constant of ZMGP (poly and mono) in comparison with ZGP. However, standard chemical phase analysis shows these lines are not sharp and cannot be accurately resolved. Therefore, the peaks associated with Mn remain stealth. All measured materials answer to the structure of chalcopyrite, space group $I\bar{4}2d$, and no secondary phases related to manganese or different crystal structures were found. Binary compounds MnP, $\mathrm{Mn_2P}$, $\mathrm{MnP_4}$, $\mathrm{Ge_2Mn_3}$, $\mathrm{Ge_2Mn_5}$, $\mathrm{Ge_3Mn_5}$, $\mathrm{Ge_5Mn_3}$, GeMn, $\mathrm{GeMn_{2.3}}$, $\mathrm{GeMn_{3.4}}$, $\mathrm{GeMn_2}$, and $\mathrm{GeMn_3}$ have not been detected. The Ge excess peaks observed in poly-ZGP were translated into poly-ZMGP without the formation of any known Ge-Mn compounds. Therefore, in the standard XRD setup, one can only assume that Mn-bound substance is present in the form of nanoscale inclusions such as nanoclusters, whose weak reflexes overlap with the strong lines of chalcopyrite.

Although the top layer exhibits metal-like properties [31,38,39], its physical nature remains unresolved, and the existence of Mn-bound nanoclusters is still debated. To clarify, we used an alternative estimate of the x-ray penetration by calculating the attenuation length L at $\lambda = 1.5406$ Å [77] for the substrate and layers (Table I) and HRXRD, Fig. 4(a).

The calculation results are given in Table I for ZGP crystal and Mn-containing materials MGP, ZMGP, and the known HM MnP [78,79]. The Mn-based materials have rather low L values regardless of the type of structural modification (tetragonal, cubic, hexagonal, or orthorhombic) in the ZMGP matrix or MnP nanoclusters. For each Mn-containing material in Table I, the x-ray absorption is stronger compared to the ZGP crystal. The $L_{\mathrm{ZGP}}/L_{\mathrm{film}}$ ratio increases with increasing [Mn], reaching a maximum value of 4.3 for orthorhombic MnP films. In the reflection mode, x rays pass through the film twice and produce ~4 times higher diffraction intensity than ZGP. Moreover, the top ZMGP layer has much higher electrical conductivity than the semi-insulating ZGP substrate (Sec. III J), so the excess of charge carriers in ZMGP is another reason for the stronger x-ray absorption in the top layers. Thus, the amplitudes of the corresponding diffraction peaks from the substrate are significantly attenuated with respect to the top layers.

To obtain more structural details, we performed precision XRD measurements in reflection mode and elucidated the quality of the crystal lattice in the endotaxial ZMGP film. Figure 4 shows HRXRD patterns for the ZMGP/ZGP specimen taken from the layer side in coupled $\omega/2\theta$ scan mode. Measurements were performed at angles $2\theta = 28°–34°$ and $70°–71°$ which correspond to the $hkl = (112)$, (004), and (008) planes.

The complex peaks were further digitally processed using Gaussian deconvolution for the two reflexes (112) and (004). The reflex (008) with nongrazing conditions was not digitally processed because the second peak (film) is expected to be of much lower intensity and out of scale at $2\theta \approx 69.96°$.

A Gaussian deconvolution model used for the (112) reflex is shown in Fig. 4(b) and for the (004) reflex is shown in Fig. 4(c). To resolve and analyze the fine diffraction structure in the HRXRD patterns, we applied asymmetric settings to reduce the beam polarization while keeping the incident beam intensity high. Due to the almost perfect nature of single crystals, peaks from the substrate often dominate the pattern [80], while peaks from films and nanoclusters have very low intensity through the lower [Mn] concentration. However, in the regime of reflection from the highly conductive layer, the ratio of peak intensities can change in the opposite way. Deconvolution of HRXRD peaks shows that three signals are clearly dominant.

Specific peaks are depicted as contours shaded in red-green-blue (RGB) colors. The maxima in Fig. 4(b) are denoted by RGB bars. The residual standard deviation Δ_0 (between data and fit) demonstrates that the pattern Δ_0 is random. The R, G peak pair appeared after endotaxial growth and belongs to Mn containing layers. The B peak answers to angles 2θ close to that from PDF cards #00–050–1210 and #01–073–0398 for ZGP [81,82].

The most intense R peak belongs to the ZMGP layer on top of the heterojunction, while the G peak at lower angles [Fig. 4(b)] and at higher angles [Fig. 4(c)] can be attributed to a transitional layer with variable low [Mn]. The intensity of the main peak for the (112) reflex at 28.469° is ∼4 times stronger than the second peak at 28.486° (ZGP substrate). This agrees with the data for the attenuation length in Table I. Note that the crystallographic (112) plane is the densest packing in the chalcopyrite structure and consists of two closely spaced cationic and anionic subplanes. For RGB peaks at the (112) reflex, FWHM = 36.9, 50.9, and 84.8 arcsec confirm the high crystallinity of the layers and, together with a small shift of 0.017° between R and B peaks, indicates that the top film has the same orientation as the interface layer and substrate.

The angular deconvolution presented in Fig. 4(c) gives FWHM = 74.9, 373.0, and 254.3 arcsec for peaks (004) larger than for peaks (112) in Fig. 4(b) (36.9, 50.9, and 84.8 arcsec). The width values indicate good crystallinity and low misorientation in the top layer, the quality of which is quite comparable with a high-quality single-crystal ZGP substrate. The larger FWHM > 200 arcsec for the ZGP:Mn transitional layer on the (004) reflex indicates the slight misorientation of nanoclusters along the [001] direction. This is consistent with the longer attenuation length in this direction (Table I), along which the lattice constants change more strongly and misorientation is more plausible.

The difference in the width parameters for reflexes (112) and (004) indicates local anisotropy in different crystallographic directions, and the peak broadening is due to a slight distortion of the local structure. Figure 4(c) shows that the weak but distinct contribution of Mn-bound nanoclusters is clearly visible on the semilogarithmic scale. The B peak at 33.422° is less intense but still well above (×108) the noise background. The G peak at 33.275° (×1220) with a broad FWHM presumably indicates the manifestation of nanoclusters in the Mn-doped ZGP:Mn diffusion layer. Partial signatures of Mn-bound nanoclusters were found in magnetotransport measurements, electron paramagnetic resonance (EPR), FM resonance (FMR), giant electron spin echo spectra [31,35–38], and tilted tetrahedron calculation from EPR data [83], and they complement our overall picture of the crystal structure with ZMGP (R peak) and ZGP:Mn (G peak) layers on ZGP crystal (B peak).

As a rule, HRXRD and rocking diffraction reflection curves have FWHM ⩽ 200 arcsec for high-quality epitaxial films of III-V compounds, indicating their good crystallinity. In the grown endotaxial layers, the width parameter points at the high crystal quality and local anisotropy. Mosaicity was not observed, and a slight broadening can be attributed to the anisotropic distribution of point defects commonly present in Bridgman-grown ZGP crystals. In this sense, Mn is also distributed with local anisotropy in the chalcopyrite lattice.

TABLE II. Lattice constants and tetragonal compression in $\mathrm{ZnGeP_2}$, $\mathrm{Zn_{1-\mathit{x}}Mn_{\mathit{x}}GeP_2}$, and $\mathrm{MnGeP_2}$.

Material	a(Å)	c(Å)	τ(%)	x(%)
ZGP[a]	5.468	10.713	2.04	0
ZGP[b]	5.465	10.711	2.00	0
ZGP:Mn[c]	5.456	10.716	1.80	>0[d]
ZMGP[c]	5.449	10.757	1.30	8
MGP[e]	5.693	11.303	0.73	100
MGP[f]	5.655	11.269	0.36	100

[a] Reference [81].
[b] Reference [82].
[c] This paper.
[d] [Mn] cannot be detected.
[e] Reference [49].
[f] Reference [24].

The lattice constants of ZMGP and ZGP:Mn layers are given in Table II. Incorporation of Mn into the ZGP crystal lattice results in a small decrease of the constant a and the simultaneous increase of the constant c at low fractions $x \leqslant 8\%$. This leads to a slight deviation from linearity of Vegard's law. The average lattice constant in the cubic approximation $a_{\mathrm{av}} = (a + c/2)/2$ gives the same value of 5.411 ± 0.003Å with good accuracy for ZGP and all ZMGP materials in Table II. This explains why previous phase XRD analyses performed by different research groups did not identify Mn-related compounds in ZMGP.

The tetragonal compression $\tau = (1 - c/2a) \times 100\%$ characterizes the unit cell using both lattice constants. Table II shows that τ decreases steadily with increasing [Mn]. The top layer of ZMGP is characterized by $x = 8\%$ with an average lattice anisotropy $\tau = 1.30\%$, which is between ZGP and MGP. The low-doped ZGP:Mn layer (G contour) is characterized by $\tau = 1.80\%$, in agreement with deeper diffusion of Mn ions. The G peak is slightly shifted toward smaller angles [Fig. 4(b)] or larger angles [Fig. 4(c)] and characterized by FWHM = 51–373 arcsec. It can be attributed to transitional layers in two different directions [112] and [001]. Obviously, it refers to materials with similar average lattice constants and high crystalline quality. All Mn-containing materials can include structural elements as $^{\mathrm{P}}_{\mathrm{P}} > \mathrm{Mn} <^{\mathrm{P}}_{\mathrm{P}}$ atomic tetrahedron. Such tetrahedra complicate the crystal structure through the formation of magnetic nanoclusters. Here, we emphasize that Mn-bound magnetic nanoclusters are not considered a secondary phase since their low concentration and phase segregation hardly exists. Thus, both crystalline and magnetic ordering in nanoclusters lead to RTFM and other magnetic effects [33,34,37,38].

According to Vegard's law, the lattice constants of the ZMGP solid solution can be fitted to a linear dependence on x, as shown in Fig. 5. Both constants a and c, determined from HRXRD measurements lead to a concentration estimate of $x = 8\%$ for the ZMGP film. A small nonlinearity is retained in this Vegard's curve, implying that manganese is anisotropically distributed in the crystal matrix. This is consistent with a weak crystallographic anisotropy in chalcopyrite SCs.

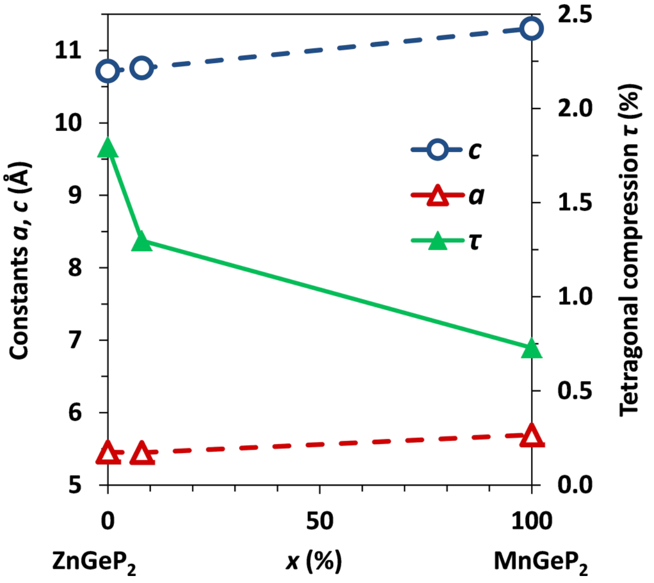

FIG. 5. Lattice constants and tetragonal compression in ZGP, ZMGP, and MGP vs $x = [\mathrm{Mn}]$.

C. Tetrahedron model

Conventional XRD phase analysis did not reveal any reliable traces of Mn-bound nanocrystalline inclusions in ZMGP or ZGP:Mn materials. Although minor MnP inclusions have been reported during epitaxial growth of $\mathrm{MnGeP_2}$ on GaAs, InP substrates [42–47] and successful suppression of secondary phases have also been reported. The AES presented above indicate the existence of Mn and P in the ~3-nm-thick outer layer with a substantial Zn drop. UPS and XPS photoemission [39] revealed a Mn bilayer profile at a depth of 110 nm, with the RTFM state preserved in both the outer and deeper layers. Since then, the presence of FM nanoclusters was used as a working hypothesis until EPR, giant electron spin echo, and magnetotransport experiments discovered the presence of Mn-bound nanoclusters in $\mathrm{Zn_{1-x}Mn_xGeP_2}$ single crystals and films [31,37,38]. Nuclear magnetic resonance in polycrystals [84] and muon spin rotation with 100% spin-polarized and positively charged muons [85] confirmed the presence of magnetic clusters in ZMGP and weakly doped ZGP:Mn. Weak field-induced FM has been measured in bulk crystals doped with Mn ($x < 5\%$) at temperatures above $T_{\mathrm{C}} = 320\,\mathrm{K}$ [85]; this FM goes to zero when the external field is turned off. MnP inclusions were also found in FM composites $\mathrm{Cd_{1-x}Mn_xGeP_2 + MnP}$ (strongly heterogeneous materials) [86,87]. Modeling of possible crystal structures of the binary MnP compound uncovered a hypothetical sphalerite modification with lattice constant $a = 5.26$ Å [79] and 5.308 Å [88]. The cubic MnP with tetrahedral coordination is constructed from manganese atoms surrounded by four phosphorus atoms, as shown in Fig. 6. Based on the data in Table I, the Mn-Mn nearest-neighbor distance is 3.859 Å for ZGP:Mn and 3.854 Å for ZMGP (8%), which is slightly larger than the calculated for MnP $d_{\mathrm{Mn-Mn}} = 3.75$ Å [88]. Details of the modeled crystal structure of sphalerite can be obtained from Refs. [79,89].

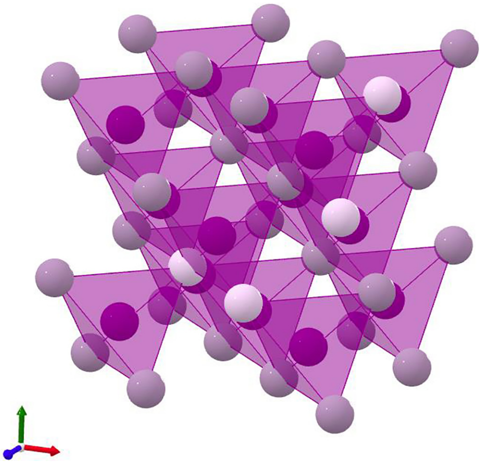

FIG. 6. Tetrahedrally coordinated crystal structure of the cubic MnP [79].

Typically, single crystals and films of MnP grow in orthorhombic or hexagonal modifications. The cubic MnP material was fairly simulated but never grown or confirmed experimentally. Structural nanofragments of the cubic MnP of the sphalerite modification with $F\bar{4}3m$ space group are suggested to be stable, but the atomic surrounding must be favorable in the first and second coordination shells. Such structural conditions are automatically realized in our Mn-doped ZGP crystals. A small difference in the ionic radii of $\mathrm{Zn^{2+}}$ 0.83 Å and $\mathrm{Mn^{2+}}$ 0.80 Å, close affinity of space groups $I\bar{4}2d$ and $F\bar{4}3m$ for two diamondlike structures, chalcopyrite and sphalerite, as well as the model of local tetrahedra $^{\mathrm{P}}_{\mathrm{P}} > \mathrm{Zn} <^{\mathrm{P}}_{\mathrm{P}}$ in ZGP [1], provide arguments in favor of a similar configuration of Mn in ZMGP.

The proposed tetrahedron model for Mn-rich ZMGP is presented in Fig. 7. Manganese coordinated tetrahedrally in the chalcopyrite lattice occupies three different cation positions in the unit cell: $\mathrm{Mn^{2+}}$ on the $\mathrm{V_{Zn}}$ site in the center, $\mathrm{Mn^{2+}_{Zn}}$ and $\mathrm{Mn^{2+}_{Ge}}$ on the Zn and Ge sites, as shown in the lowest plane of the unit cell. The ionic-covalent bonds form three tetrahedra: one anionic $^{\mathrm{P}}_{\mathrm{P}} > \mathrm{Mn} <^{\mathrm{P}}_{\mathrm{P}}$ and two cationic $^{\mathrm{Zn}}_{\mathrm{Mn}} > \mathrm{P} <^{\mathrm{Ge}}_{\mathrm{Mn}}$. The last tetrahedron is important for the explanation of FM, where the acceptor $\mathrm{Mn^{2+}_{Ge}}$ provides two holes to contribute to hole mediated FM exchange between $\mathrm{Mn^{2+}_{Zn}}$ and $\mathrm{Mn^{2+}_{Ge}}$.

Magnetic interactions occur between zero, second, and fourth neighbors in cationic tetrahedra through intermediate P anions. Anion-cation bonds forming chains ($\mathrm{Mn^{2+}_{Zn}}$-P-$\mathrm{Mn^{2+}_{Ge}}$) and ($\mathrm{Mn^{2+}_{Zn}}$-P-$\mathrm{Mn^{2+}_{Ge}}$-P-$\mathrm{Mn^{2+}_{Zn}}$) were proposed in Refs. [37,38] to interpret EPR, Hall effect, and magnetoresistance experiments in ZMGP. In parallel, a theory of practical rules for orbital-controlled FM of 3*d* impurities in SCs was developed [90]. The theory stated that FM interaction exists only along the [110] chain direction. In the [001] direction, FM is weak because of less $t_2 - t_2$ orbital overlap for geometric reasons and can compete with AFM. The theory considering only the II site for substitution, Mn → Zn or Mn → Cd [23,24], concluded that the AFM state is preferable. A theoretical approach [20,90] considered double substitution at the II and IV sites and found that the magnetic interaction is preferable to FM. Therefore, our model in Fig. 7 shows both predicted

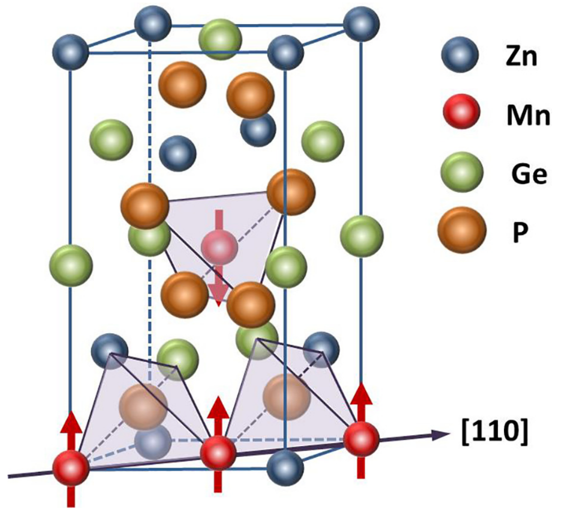

FIG. 7. Tetrahedron model of ZMGP chalcopyrite lattice with embedded tetrahedra $^{\mathrm{P}}_{\mathrm{P}}> \mathrm{Mn}_{\mathrm{Zn}} <^{\mathrm{P}}_{\mathrm{P}}$ and $^{\mathrm{Zn}}_{\mathrm{Mn}}> \mathrm{P} <^{\mathrm{Ge}}_{\mathrm{Mn}}$. Two different Zn cations and one Ge cation sites occupied by Mn ions having magnetic moments ferromagnetically (FM) aligned in the [110] direction, and one of them antiferromagnetically (AFM) aligned in the [001] direction.

orderings for tetrahedrally coordinated $\mathrm{Mn}^{2+}_{\mathrm{Zn}}$ and $\mathrm{Mn}^{2+}_{\mathrm{Ge}}$ ions: AFM ordering along the [001] and FM ordering in the [110] directions. Thus, the tetrahedron model with chains explains the experiment and is confirmed by theories.

Crystallographic anisotropy in undoped ZGP crystals due to nonequivalent $\mathrm{P_A}$-Zn-$\mathrm{P_A}$ and $\mathrm{P_C}$-Zn-$\mathrm{P_C}$ atomic bonds [91–93] leads to tetrahedron deformation and local optical anisotropy [1]. After Mn → Zn substitution, a similar deformation is expected in Mn-bound tetrahedron $^{\mathrm{P}}_{\mathrm{P}} > \mathrm{Mn}_{\mathrm{Zn}} <^{\mathrm{P}}_{\mathrm{P}}$ due to asymmetric Mn-P bonds. The formation of more extended nanoclusters overlapping neighboring unit cells is also likely in several configurations: two or three or more neighboring tetrahedra may combine to form larger FM clusters. The embedded nanoclusters do not distort the lattice as a whole, but there are local distortions due to different bond lengths of $\mathrm{P_A}$-Mn-$\mathrm{P_A}$, $\mathrm{P_B}$-Mn-$\mathrm{P_B}$, and $\mathrm{P_C}$-Mn-$\mathrm{P_C}$, like those in the ZGP crystal [91–94]. The net magnetization of nanoclusters bound via hole-spin exchange can be further sensitive to the applied magnetic field, and their magnetic moments can align along the external field [85].

D. Heterojunction layer structure

A schematic of the measured heterojunction samples with electric contacts is depicted in Fig. 8(a). The bilayer model of the Mn-rich ZMGP and Mn-poor ZGP:Mn layers is shown with a color gradient in depth to delineate the manganese distribution profile. Au contacts were used to take the low-frequency modulated photoresponse U_{ph} in two illumination geometries (front and back). The contacts were shaded to avoid parasitic photogeneration of excess charge carriers. Light incident from opposite directions $(1 - R_1 + R_2)$ and $(1 - R_3)$ generated the spectral photoresponse due to different photoactive absorption in the depletion region and in the bulk substrate, respectively.

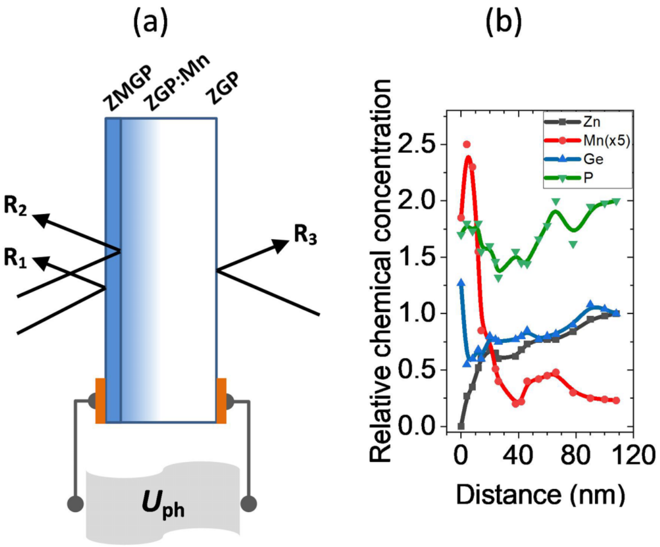

FIG. 8. (a) Cross-sectional sketch of ZMGP/ZGP heterojunction with three principal optical reflections R_1, R_2, and R_3 from different surfaces of the structure. Photoresponse U_{ph} was measured in two opposite geometries corresponding to the reflection conditions $(1 - R_1 + R_2)$ and $(1 - R_3)$. (b) Chemical concentration distribution in depth for Zn, Mn, Ge, and P components; the [Mn] (red line) is multiplied by the factor of 5.

Figure 8(b) gives the relative chemical concentrations measured for the elements Zn, Mn, Ge, and P according to Ref. [39]. The used sputter-etching rate is 2 Å/min. The manganese profile follows an exponential decay with >1 exponent. A distinctive feature of this distribution is that the ~50% maximum is near the surface, while [Mn] decreases slightly at the very surface and strongly in depth. Such a profile in the endotaxial film is like that of low-energy implantation but differs from that of gas-phase doping. The ZMGP/ZGP:Mn interface appears sharp since the Mn-rich and poor layers have high and low electrical conductivity [31], and in the Cd analog, the Mn bilayer also appears clearly [34,48]. The [Mn] line in Fig. 8(b) shows two regions, Mn rich ($x \sim 0.5$, $d = 15$ nm) and Mn poor. The deep layer has an exponential decrease in manganese concentration with $x = 0.1$ at $d = 52$ nm and $x = 0.045$ at $d = 94$ nm. The rest of the sputter-stripped off film has a low concentration [Mn] ≈ 4.5% detected at $d = 110$ nm.

Within the thin plate approximation with multiple optical reflections and without interference effects, we use the optical model [95] with two reflected rays, Fig. 8(a). This model can be applied since the optical reflection inside the crystal from its back surface can be neglected. It is assumed that the optical constants of the low-doped diffusion layer coincide with those of the substrate, at least in the mid-IR range of interest. Using front- and back-probing optical beams and the bilayer model, we directly obtained optical band gap and reflection data of the ZMGP layer to characterize its fundamental optical edge and deep fundamental band.

E. Optical transmission in the mid-IR

The optical transmission spectra for undoped $\mathrm{ZnGeP_2}$ single crystals, the ZMGP/ZGP heterojunction, and ZMGP film

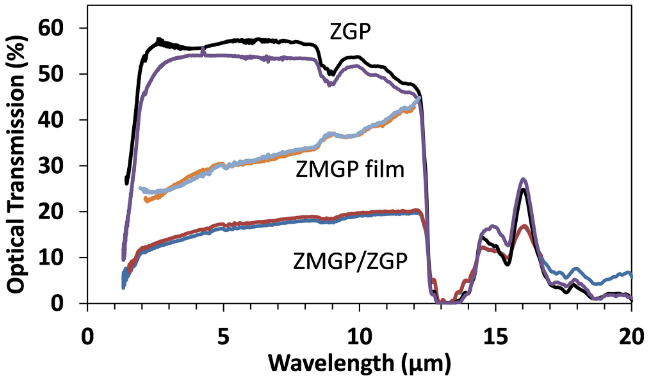

FIG. 9. Optical transmission of $ZnGeP_2$ undoped crystal, ZMGP film, and ZMGP/ ZGP heterojunction. The curves are of two crystals and two heterojunctions.

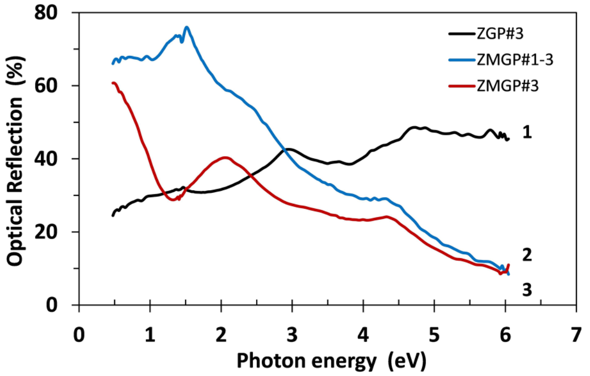

FIG. 10. Optical reflection of $ZnGeP_2$ undoped crystal (1) and two heterojunctions with ZMGP top layers grown on $ZnGeP_2$ under different conditions (2) and (3).

in the range of 1–20 μm are shown in Fig. 9. Two samples ($d = 1.2$ mm) have a fairly close spectrum shape, and the absolute transmission differs by a few percent. Difference in the average T amplitude within the operation window (2–12.5 μm) in one crystal is ∼3% greater than in the other, while in the far infrared range (14–19 μm), it is opposite, $T_1 < T_2$. This small discrepancy may be caused by different cuts along the ingot or slight differences in surface polishing and thickness variance. In general, the optical transmission spectrum corresponds to the best ZGP crystals without antireflective coating.

Optical transmission measured in the ZMGP/ZGP heterojunction is lower, $T_{\text{aver}} = 15$–20%, than in the bare ZGP crystal, although the optical quality of ZMGP layer is good enough and acceptable for optical measurements. This reduction is associated with two optical effects as the higher absorption in the ZMGP layer and the higher reflection from the ZMGP surface. To obtain the transmission coefficient for ZMGP film itself, we divided the heterojunction transmission by the crystal transmission $T_{\text{hj}}/T_{\text{cr}}$.

The resulting curves are given in Fig. 9 for two films. The transparency window 2–12 μm is characterized by relatively high values of $T(\lambda)$ and increased dispersion $dT(\lambda)/d\lambda$ compared with the crystal and heterojunction. At the edges of this window, the spectral dispersion turns into a fast function, and the spectral error increases, so these edges have been omitted for simplicity. In the window interval, the optical transmission of ZMGP is rather high $T = 22$–45%. This indicates that heavy Mn doping reduces the overall transparency of ZMGP but not as dramatically as expected and, importantly, does not lead to the formation of any absorption bands within the transparency window. This agrees with the optical transmission data of ZGP crystals doped with low Mn content [96]. At first glance, ZMGP layers can be utilized in the development of magneto-optical media based on the nonlinear optical crystal ZGP with properly designed antireflective coatings on top of ZMGP.

F. Optical reflection

Figure 10 shows the optical reflection spectra of the original undoped $ZnGeP_2$ crystal and two ZMGP/ZGP heterojunctions ($T_{\text{dif}} = 400$ and 550°C) measured from the layer side at $T = 300$ K.

The reflection spectrum for the undoped crystal (Fig. 10, curve 1) is like the previously reported most reliable measurements published in the past five decades [97,98]. For the spectral measurements, we followed the same proper surface preparation. Without final polishing and etching, the reflection structure was generally not as high and sharp, but no additional features appeared for ZGP crystals compared with those known [97,98]. The additional data for ZMGP are presented in Fig. 10 by curves 2 and 3. They demonstrate a large spectral difference in the reflection amplitude and spectral distribution throughout the mid-IR range. Their spectral peaks, amplitude, and the sign of the spectral dispersion $dR/d(\hbar\omega)$ are dissimilar. The sign of the dispersion indicates that the top ZMGP layers are not a conventional SC with low to medium hole concentration like DMS ZGP:Mn but a material with metallic behavior. Values of $R = 25.2\%$ (ZGP), 66.8% (ZMGP #1), and 60.6% (ZMGP #3) were measured in the low-energy portion of the spectrum and used in the calculation of the optical absorption coefficient from T spectra in the near and mid-IR (Sec. III H).

The spectral structures in Fig. 10 differ significantly in shape, amplitude, and photon energy depending on the growth technology of layers. The dominant maxima at 1.59 eV (curve 2) and ∼0.5 eV (curve 3) have not been previously observed in SCs with low to medium electron/hole concentrations. The reflection amplitude for both ZMGP layers increases to 61–76%, light penetrates the region with low Mn concentration, and the difference in R amplitude indicates different diffusion distribution of Mn. Furthermore, curve 3 at energies between 0.5 and 2.5 eV clearly shows the spectral shape characteristic of a metal or a heavily doped narrow-gap SC, when $n \approx k$ and a clear minimum at 1.33 eV is associated with a plasma frequency ω_p. The dependence can be described by the simple Drude theory for metals and the Drude-Lorentz model [99,100]. However, unlike pure metals, the amplitude R does not reach 100% at maximum and does not drop to 0% at ω_p. These signs are in favor of HM. Indeed, the known FM HMs show a similar spectral shape of reflection and plasma minima at $\hbar\omega_p = 1.49$ eV (CrO_2) [101,102], 0.82 eV (Co_2TiGe, Co_2TiSn Heusler Alloys) [103], and $1.6 - 6.1$ eV (NiMnSb, PdMnSb, PtMnSn, PtMnSb, and CuMnSb) [104].

In the visible (VIS) and near-ultraviolet (UV) bands (3–6 eV), light is reflected from the uppermost part of the

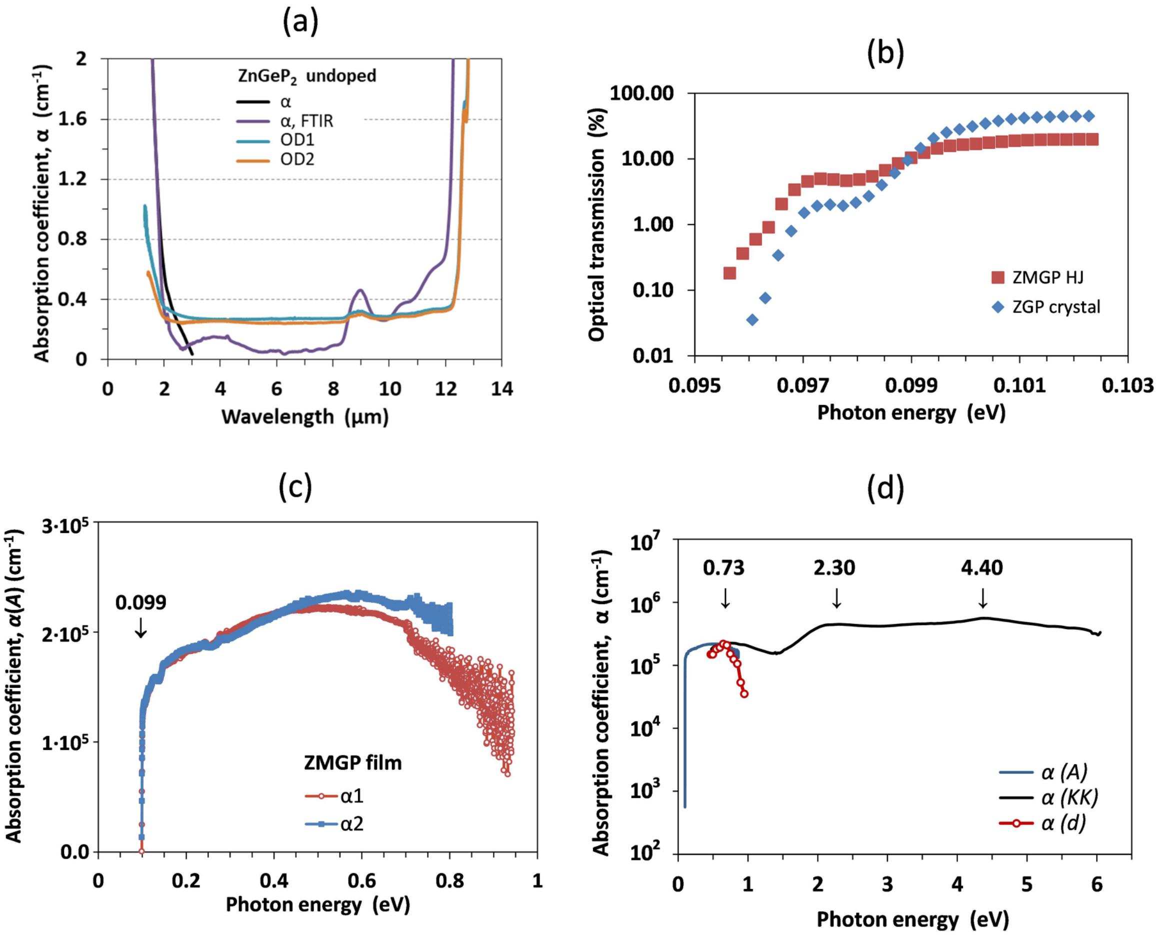

FIG. 11. Optical spectra of ZnGeP$_2$ crystals and ZMGP/ZGP heterojunctions at $T = 300$ K. (a) Midinfrared (mid-IR) absorption of ZGP undoped crystals. Notations: α is by classic spectral and Fourier transform infrared (FTIR) measurements; OD is by optical density (or A). (b) Transmission spectra for ZMGP/ZGP heterojunction and ZGP clear crystal. (c) Edge absorption of ZMGP, two film samples. (d) Fundamental absorption band of ZMGP. Blue curve is $\alpha(A)$ measured by absorbance; black curve is α(KK) by Kramers-Kronig transform; red dots are $\alpha(d)$ by calculation with Eq. (2), and T, R data, and d as a fitting parameter.

layers and brings information from shallower depths where the Mn concentration is maximal. Curves 2 and 3 in Fig. 10 are distributed closer to each other with similar spectral patterns at energies ~2.1, 3.5, and 4.3 eV, and the optical depth αd becomes comparable in two samples. These features indicate the chemical composition and Mn content are similar in both upper ZMGP layers. No interference effects are observed in this spectral interval.

The relationship between the optical and electrical properties of solids via the conductivity tensor makes the highly reflective material also a fairly good electrical conductor, so the spectra in Fig. 10 indicate a high electrical conductivity of ZMGP layers. Magnetotransport of holes in ZMGP [31,38] is in line with this finding.

G. Optical absorption and optical density

Figure 11(a) shows the mid-IR optical window (2–12.5 μm) measured on several undoped ZnGeP$_2$ crystals, $T = 300$ K. The spectral data were used to determine the fundamental optical edge of ZMGP in the ZMGP/ZGP heterojunction. For samples grown by the vertical Bridgman method, spectra obtained on classical double-beam and IR spectrophotometers were compared, after which the T spectra were converted to optical density (OD) or absorbance (A) spectra. To calculate the optical absorption coefficient α from the T and R data (Figs. 9 and 10), the two-beam reflection model [95] was used:

$$T = \frac{(1 - R_1)(1 - R_2)\, e^{-\alpha d}}{1 - R_1 R_2\, e^{-2\alpha d}}, \tag{2}$$

where R_1 and R_2 are reflections at the frontal and interface surfaces, Fig. 8(a). Equation (2) is used in the absence of interference effects associated with multiple reflections inside the crystal plates, and we can simply add up the intensities of the two reflected rays.

Both ZMGP and ZGP:Mn layers satisfy this condition since the ZMGP layer is much thinner than the diffusion layer, and ZGP:Mn has optical parameters very close/equal to those of the undoped substrate in the mid-IR. While the minimum absorption coefficient α in Fig. 11(a) measures as $\alpha = 0.2$ cm^{-1} at $\lambda = 2$ μm and 0.07 cm^{-1} at $\lambda = 5$ μm, the absorbance (A) gives a value of >0.2 cm^{-1}. This difference in amplitude was accounted for, but the other features of the spectrum were not significantly affected. The measured crystals are in good agreement with the best nonlinear optical ZnGeP$_2$ crystals, but the lowest absorption coefficient at $\lambda = 2$ and 5 μm can be achieved in samples designed for special applications.

The α/A ratio with a factor of ~3.5 at 5 μm was used to estimate the absorption coefficient in the standalone ZMGP film from measurements of A. Note that the absorption coefficient at the window boundary at 2 μm strongly depends on the concentration of Zn vacancies, and its sharp reduction is the goal of numerous attempts to ensure the best possible performance of nonlinear optical devices in the mid-IR [1–3]. The peak at 9 μm in Fig. 11(a) is associated with three-phonon absorption. At longer wavelengths, the transparency window ends with a sharp increase in absorption at 12–13 μm. This spectral range is still under investigation for possible intrinsic point defects in undoped $ZnGeP_2$, and here, we underline its particular importance for heavy manganese doping.

H. Fundamental absorption band in ZMGP

Seeing that the edge absorption coefficient and OD curves diverge at 12–13 μm [Fig. 11(a)], we performed spectral scans of the heterojunction and bare uncoated $ZnGeP_2$ crystal using crystal plates of the same thickness (1.2 mm) to minimize spectral errors in measurements on the same FTIR instrument. The spectral range of particular interest is shown in Fig. 11(b) for both the heterojunction and clear crystal. The optical transmission varies from $T = 10$ to 45% and is accurate and reliable because the spectrometer detector signal far exceeds the background noise. Each measured curve was converted to an OD curve, and the resulting OD spectra were subtracted from each other (since α and OD are additive functions, unlike T).

In this paper, optical properties of ZMGP solid solution were measured. The energy band structure was modeled using various theoretical approaches [18,23,26,30]. In the chalcopyrite II-IV-V_2 group, 21 stable FM compounds were identified [18], which are idealized HM at zero temperature and for an ordered arrangement of Mn atoms, with electronic states at the Fermi level in only one spin channel. Refernce [21] reported that both $ZnGeP_2$: Mn and $CdGeP_2$: Mn become HM at Mn concentration $x = 0.2$, and the plausible chemical formulas are $(Zn_{0.8-x}Mn_{0.2}V_{Cx})GeP_2$, $(Zn,V_C,Mn)GeP_2$, or $(Zn,Ge,Mn)GeP_2$, where the cation vacancy $V_C = V_{Zn}$. Other theoretical models [25,28–30] also support the possibility of the existence of a HM state in ZMGP, $MnGeP_2$, or a SC state with a nonzero band gap. HM was calculated in chalcopyrite compounds $ZnXP_2$, where $X =$ Sc, V, Cr, or Fe; however, the main substitution Mn_{Zn} was ignored [29]. Some of the above theories are closer to practice; others are not. In this paper, we provide experimental arguments optically supporting the presence of HM in the diamondlike material ZMGP.

To achieve spectral accuracy, we spectrally separated the top layer of ZMGP from the endotaxial heterojunction grown on the ZGP seed crystal. This standalone layer was treated in terms of measured T, R data and Eq. (2). The conversion of the absorbance A data to the absorption coefficient α in the range where no R data are available was performed using the Bouguer-Beer law:

$$T = \exp(-\alpha d), \tag{3}$$

$$\alpha = \frac{\Delta A}{d \times \log_{10} e}\ [\text{cm}^{-1}], \tag{4}$$

where the absorbance in the layer $\Delta A = \log_{10}(1/T_{\text{hj}}) - \log_{10}(1/T_{\text{cr}})$, and d is the film thickness. The amplitude in cm^{-1} for the $\alpha(A)$ spectrum was correlated in amplitude with the Kramers-Kronig transform data in the 0.5–6 eV range.

Figure 11(c) shows the optical absorption spectra of two ZMGP films obtained from the absorbance data. The high-energy ends in the spectra have scattered points due to the finite Fourier transform and can be neglected. We show these points to demonstrate the trend of the absorption coefficient at energies >0.7 eV. The overall shape of the spectra is almost the same for ZMGP films in both heterojunctions.

The sharp edge is identified at 0.099 eV. This can be attributed to the beginning of interband optical transitions in ZMGP film since the absolute optical absorption reaches $\alpha > 10^5\ \text{cm}^{-1}$ and the spectral contour is like the SC compounds with a direct band gap. Two reasonable options can be considered: a HM or a SC with a very narrow band gap. The existence of the HM is consistent with the above simulations and experiments on hole transport, electrical conductivity, and anomalous Hall effect [31,38].

Figure 11(d) shows the optical absorption spectra overlapping the broader IR-VIS-UV spectral ranges. The experimental data in this fundamental absorption band consist of the following contributions: (1) $\alpha(A)$, from absorbance of the spectrally separated ZMGP film; (2) $\alpha(KK)$, from the Kramers-Kronig transform; and (3) $\alpha(T,R)$, from Eq. (2). Whereas the KK equations use only R data, the absorbance equations use T data, so the thickness d was used as a fitting parameter. The calculation of $\alpha(T,R)$ was performed using T and R data only available in the narrow range of 0.47–0.80 eV (red dots).

The best fit $d = 15.5$ nm for the ZMGP layer was obtained with Eq. (2). This thickness seems reasonable since the 50-nm-thick Mn metal layer serves as a source for the growing solid solution layer and thicker Mn-poor layer. This thickness agrees with that measured directly for the layer-by-layer stripping technique, Fig. 8(b) and Ref. [39]. In $CdGeP_2$ (112), manganese penetrates deep in the crystal (~2.6 μm), forming an extended Mn-poor layer of $CdGeP_2$: Mn [10,11], but in $ZnGeP_2$ (001), manganese diffuses less deeply because of the different crystallographic direction. Given that diffusion coefficients are different for Si wafers with (001) and (111) planes, it is logical to assume that the (001) and (112) planes in diamondlike chalcopyrite have similar diffusion behavior. Thus, a thinner ZMGP film in the [001] direction is reasonable.

The SC band gap $E_g = 0.099$ eV at 300 K looks very narrow, but compared with the thermalization energy $kT = 25.9$ meV, it is wide enough that holes cannot overcome the band gap at RT. Clearly, the presence of point-defect levels in the band gap of ZMGP can allow for multistep transitions of holes into the valence band. When a certain percolation threshold is reached, the electrical conductivity becomes high, as in metal.

The fundamental absorption band is characterized by the principal peaks marked with arrows. The maxima at 2.30 and 4.40 eV refer to the transitions associated with Mn in ZMGP since they are also observed in the reflection spectra, Fig. 10. The intrinsic absorption in ZMGP is superimposed on the impurity absorption in the wide-gap ZGP crystal. The peak at 0.73 eV falls within the spectral interval responsible for optical transitions involving the deep levels of intrinsic point defects in ZGP substrate [1]. The high absorption of $\alpha \sim 2\times10^5$ cm^{-1} at 0.73 eV may indicate the presence of predominant V_{Zn} point defects in all layers of the heterojunction. After the Mn → Zn/Ge substitution, additional impurity defects Mn_{Zn}, Mn_{Ge} can pair with the remained V_{Zn}, forming the defect pairs or cluster complex.

The sharp growth in optical absorption in Figs. 11(c) and 11(d) is associated with the fundamental absorption edge in the narrowest-gap component of the ZMGP/ZGP heterojunction. This shape is characteristic of SCs with diamondlike crystal structure. The absorption coefficient $\alpha(\hbar\omega)$ quickly reaches the value $\alpha \approx 1.5\times10^5$ cm^{-1} at the spectral bend of 0.099 eV and then gradually increases to 2.3×10^5 cm^{-1}, peaking at 0.73 eV. The absolute value α is consistent with the fundamental absorption in III-V, II-VI, II-IV-V$_2$, and I-III-VI$_2$ direct-gap SC compounds, but the increase of α in the interval up to 6 eV is much slower. The featured absorption in ZMGP testifies to the strong influence of HM. While electrical evidence of HM was obtained in Ref. [31], this paper presents optical evidence of HM in ZMGP.

I. Fundamental absorption edge in ZMGP

After Mn incorporation, the optical absorption coefficient near E_g increases by a factor of 10^3 compared with the undoped crystal. This asserts a different origin of absorption in ZMGP in contrast with ZGP, where the minimal optical transitions are pseudodirect. Although the shape of the absorption curve in the impurity/point-defect spectral range may be like the fundamental band edge (e.g., in Mn-doped Ge), the matrix element of interband transitions exceeds that of D-A, VBM-D, and A-CBM transitions by >2 or 3 orders of magnitude, indicating the direct band gap character of the *p*-ZMGP solid solution. The SC part of the HM can be described by means of the energy band model in the parabolic approximation according to Moss *et al.* [100]. The absorption edge in direct SCs with parabolic bands is described by theoretical dependences:

$$\alpha = \alpha_0 \frac{(\hbar\omega - E_g)^{1/2}}{\hbar\omega}, \tag{5}$$

$$\alpha = \alpha_0 (\hbar\omega - E_g)^{1/2}, \tag{6}$$

where α_0 is a function depending on the matrix element of transitions and is usually a weak function of the photon energy $\hbar\omega$. Applying the modeling approaches, we plotted the absorption coefficient spectra of the experimental and calculated curves in Fig. 12 using Eqs. (5) and (6). The extended range 0.09–1.1 eV is shown in Fig. 12(a); the magnified details in the vicinity of E_g are shown in Fig. 12(b). The dashed black lines [Eq. (5)] and dotted green lines [Eq. (6)] are plotted with the following constants: $E_g = 0.099$ eV, $\alpha_0 = 8\times10^4$ cm^{-1}, and 2×10^6 cm^{-1}, respectively.

The parabolic band approximation, in general, agrees well with the experimental spectrum at photon energies close to E_g, and the divergence appears at higher energies $> 3E_g$. This behavior is characteristic of SCs with a direct band gap since the transition matrix element $|p_{mo}|$ in the model decreases with increasing photon energy. The introduction of an additional rising factor $f(\hbar\omega)$ allows the function $f(\hbar\omega)\ |p_{mo}|^2/\hbar\omega$ to be practically constant over the extended range.

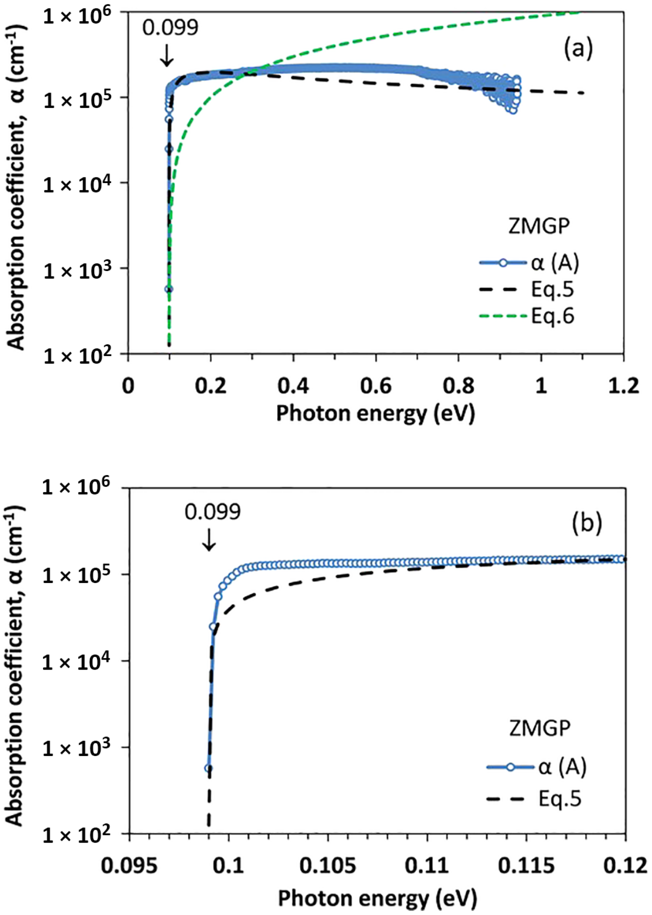

FIG. 12. Parabolic approximation for the fundamental absorption edge of ZMGP film (sample #3). (a) Wide-range fit by Eqs. (5) and (6). (b) Band gap details near the E_g energy.

Let us draw an optical analogy with linearly polarized light. Measurements in linearly polarized light lead to splitting and sharpening of polarized structures in the absorption spectra. For example, a sharper fundamental edge appears in $CdSiAs_2$ and $CdSnP_2$ crystals in the polarizations $\vec{E} \parallel \vec{c}$ and $\vec{E} \perp \vec{c}$ compared with the binary analogs GaAs and InP without excitonic effects [105,106]. The absorption edge in Fig. 12(a) is sharp and looks like the ones mentioned above, and the valence band in the ZMGP compound should be split for spin-polarized holes due to the HM state. Carrier polarization simulations [28] showed that, in ZMGP, the valence band is split into states with spin up and spin down, at least at $x = 6\%$. A similar effect, but for linear polarization of light, is observed in SCs II-IV-V$_2$, where the valence band is split by spin-orbit and tetragonal crystal-field interactions, and the two absorption edges diverge from each other, ending in sharper spectral steps at $\hbar\omega_A \equiv E_g$ and $\hbar\omega_B$ [107].

The narrow band gap may be the reason for the high electrical conductivity in the upper ZMGP layer since the gap is only $3.9\times kT$, and thermal excitation of charge carriers into a free continuum is very probable at RT. Moreover, such an intriguing combination does not rule out a wider band gap in the

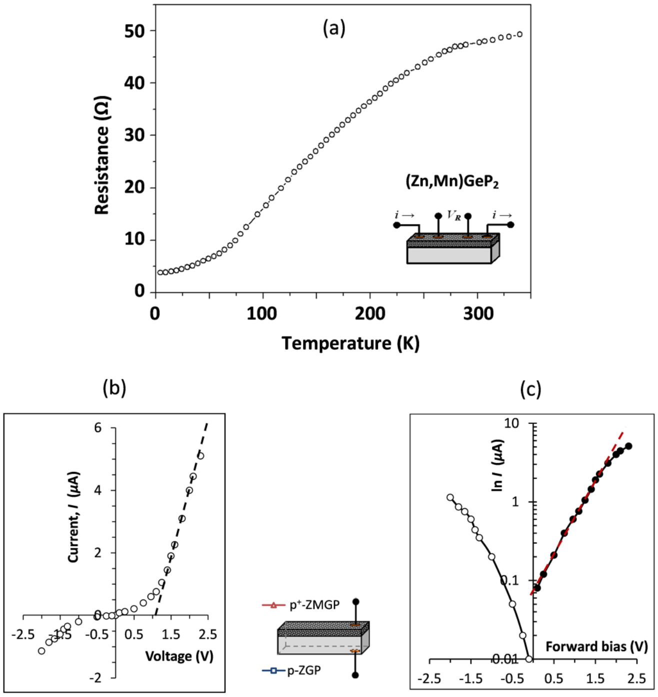

FIG. 13. Electrical transport measurements in two geometries shown in the upper and lower panels. (a) Temperature dependence of the electrical resistance of ZMGP layer; the tetragonal axis $\vec{c}$ is perpendicular to the layer plane. (b) *I*-*V* characteristic for ZMGP/ZGP Schottky type diode in linear scale. The cutoff voltage is 1.02 V. (c) *I*-*V* characteristic for ZMGP/ZGP Schottky type diode in semilogarithmic scale. The cutoff current is 0.07 μA.

SC channel of this HM or high-energy intracenter transitions in Mn ions. This issue can be probed by excitation of radiative recombination as was previously done in (Cd,Mn)GeP$_2$ [108,109]. To understand why the increasing [Mn] leads to a decrease of the band gap, we set up electrical measurements of the ZMGP top layer and the current transport through the heterojunction.

J. Electrical resistivity

Thermal probe measurements showed that the major charge carriers in both ZGP and ZMGP are holes. The highly conductive Mn-rich p^+-ZMGP layer was grown on semi-insulating p-ZGP substrate with a resistivity $10^6 - 10^7\ \Omega\,\text{cm}$. The average hole concentration in the single-crystal substrate is $p \approx 10^{14}\ \text{cm}^{-3}$ at RT, so the effect of the substrate on the electrical resistivity of the upper layer was reliably negligible. The four-point scheme with Au-dot contacts on the ZMGP top layer was used to measure electrical resistivity $r(T)$. Figure 13(a) shows the temperature dependence of electrical resistance for the Mn-rich p^+-ZMGP layer. The specimen was steadily cooled from 350 to 4.2 K.

The dependence of resistivity $r(T)$ is characteristic of metallic materials without any sign of SC component. We estimated the electrical resistivity using the layer thickness of 15.5 nm. The value for ZMGP was $\rho = 0.37\times10^{-4}\ \Omega\,\text{cm}$ at RT. This resistivity is slightly higher than that of typical single-element metals or metal alloys $\rho = 10^{-4} - 10^{-6}\ \Omega\,\text{cm}$ and slightly lower the pure metal Mn $\rho = 1.5\times10^{-4}\ \Omega\,\text{cm}$ at $T = 300$ K [110,111]. The resistivity of Mn-rich ZMGP is also comparable with the RT values for FMHM compounds MnP and CrO$_2$ $\rho = 2.0\times10^{-4}$ to $3.5\times10^{-4}\ \Omega\,\text{cm}$ [112–116] and Co$_2$MnSi $\rho = 0.16\times10^{-4}\ \Omega\,\text{cm}$ [117].

The residual resistivity ratio (RRR) $\rho_{300\,\text{K}}/\rho_{4.2\,\text{K}} = 6.7$, which is twice as large in comparison with a Heusler compound Co$_2$MnSi film [118] and like that of single-crystalline Co$_2$MnSi [119,120]. The lowered RRR is usually associated with a negative contribution to the resistivity from lattice point defects and atomic disorder at the interface. This leads to a reduction of spin polarization in Co$_2$MnSi from 93 to 55% when comparing epilayers with polycrystalline ones [120,121]. The high RRR factor in ZMGP further confirms the single-crystal nature of the grown endotaxial films.

K. $I - V$ characteristics

The dark *I*-*V* characteristics were measured at $T = 300$ K using U_{ph} contacts [Fig. 8(a)], and results are presented in Fig. 13, bottom panels. The Au-dot contacts demonstrate satisfactory ohmic properties on both parts of the heterojunction, and rectification is due to the presence of the $p^+ - p$-type junction. This junction exhibits the behavior of the metal-SC energy barrier, and the HM ZMGP layer serves as a metal rectifying contact. Nine orders of magnitude difference in resistivity between the top layer and the crystal leads to a broadening of the depletion region from the interface entirely inward the SC, mostly the low-doped ZGP:Mn layer. The charge distribution is typical of a Schottky-type barrier, so a thermionic-emission model was applied to the measured diode.

In Fig. 13(b), the forward branch of the *I*-*V* curve has a linear portion at $V > 1.4$ V, indicating the high-resistance effect by the p-ZGP substrate, which constrains the current flow across the heterojunction. The residual resistance of the crystal is estimated as $2.6\times10^5\Omega$ at $T = 300$ K. In terms of the current flowing through the diode, the charge carriers pass predominantly above the barrier at this bias. At voltages applied across the diode $V_{\text{D}} > 3kT/q$, the simple expression $V_{\text{D}} = V - IR_0$ is executed; here, V is the total voltage drop across the series combination of the diode and the resistor.

The cutoff voltage for the linear portion of the *I*-*V* characteristic gives a value of 1.02 V, which coincides with the barrier height $q\,\varphi_{\text{B}} = 1.02$ eV at the interface (see Sec. III L). A soft breakdown observed on the reverse branch is due to dark current leakage through the barrier (presumably due to inhomogeneity of the junction and surface leaks).

In Fig. 13(c), the portion in the middle part of the forward branch obeys an exponential dependence of I on V at biases 0.2–1.7 V. This electrical current is limited by the $e - h$ recombination in the space-charge region, which is located in the low-doped ZGP:Mn layer. The corresponding current cutoff is $I_{\text{S}} = 0.07\ \mu\text{A}$. At higher forward bias >1.7 V, the diode current is affected by recombination in the quasineutral region. The beginning of such a charge transport is seen in Fig. 13(c) at higher biases. The leakage increases with increasing V, which is most likely due to the presence of deep levels in the band gap of ZnGeP$_2$.

Then we extracted the main Schottky diode parameters using the techniques described in Ref. [122]. In the Schottky barrier approximation, the current through the HM/SC contact has the following form:

$$I = A_{\text{eff}}A^{**}T^2 \exp\left(-\frac{q\varphi_B}{kT}\right)\left[\exp\left(\frac{qV_D}{nkT}\right)-1\right], \quad (7)$$

where A_{eff} is the effective area of the diode, A^{**} the effective Richardson constant, T the absolute temperature, φ_{B} the barrier height of the Schottky diode, q the electron charge, V_{D} the voltage applied across the diode, n the ideality factor, and k the Boltzmann constant. The multiplier $A_{\text{eff}}A^{**}T^2$ has the meaning of the saturation current $I_{\text{S}} = J_{\text{S}} \times A_{\text{eff}}$. The extrapolated value of current density J_{S} at zero voltage gives the barrier height according to the equation [122]:

$$\varphi_B = \frac{kT}{q} \times \ln\left(\frac{A^{**}T^2}{J_S}\right). \quad (8)$$

In the simple approximation of free electrons with effective mass $m^* = m_0$, the calculated effective Richardson constant is 120 A/cm^2 K^2 [123,124], and the barrier height in ZMGP/ZGP equals $\varphi_{\text{B}} = 1.035$ eV (in q-charge units, eV). The common trend for p-type SCs vs n type is a lower value of A^{**} (e.g., for p-Si, the constant $A^{**} = 32$ A/cm^2 K^2 is $\sim$3 times lower than for n-Si). The experimental value for holes measured in $p-\text{ZnGeP}_2$ crystals is $m_{\text{h}}^* = (0.5 \pm 0.1)m_0$ [125] and $A^{**} = 60$ A/cm^2 K^2. However, the effective Richardson constant in ZMGP film is different, and according to Ref. [126], the metallic spin direction in FMHM with sphalerite/zinc-blende structure shows conduction in very wide bands with an effective mass approximately equal to the free electron mass. Thus, the estimate $\varphi_{\text{B}} = 1.035$ eV from the *I-V* characteristic of the p^+-ZMGP/p-ZGP heterojunction is considered correct. This estimate can be compared with φ_{B} measured by the independent photoemission method as shown below.

Finally, the ideality factor n was obtained using the equation [122]:

$$\frac{dV}{d(\ln J)} = RA_{\text{eff}}J + \frac{nkT}{q}. \quad (9)$$

The linear plot of $dV/d(\ln J)$ vs J gives RA_{eff} as a slope and nkT/q as the y-axis intercept. The obtained ideality factor $n = 1.16$ in the ZMGP/ZGP diode is fairly low. The ideality factor close to unity means that the current is generated by thermionic emission, and carrier leakage and tunneling through the traps are insignificant. Furthermore, Schottky contact inhomogeneity associated with larger $n = 1.2 - 2.0$ has been observed in some Si and GaN diodes [127], but in this device, the lower value of n indicates good uniformity of the ZMGP/ZGP junction.

L. Photoemission in Schottky barrier

Given that HM p^+-ZMGP film acts as a Schottky barrier, IPE of holes occurs when the illumination is turned on. We studied the spectral photoresponse in the range of photon energies 1.0–4.0 eV at $T = 300$ K. The photoresponse signal was normalized by an equal number of incident photons to obtain the quantum efficiency η in arbitrary units. The spectral results in the two illumination geometries are presented in Fig. 14(a). Minimal optical transitions in ZnGeP$_2$ are pseudodirect A′, B′, C′ and direct A, B, C; they are denoted by arrows. High-energy direct transitions from E$_1$ to E$_6$ are marked deep in the fundamental absorption band. No drop of $\eta(\hbar\omega)$ was observed in the high photon energy range, indicating very low or no surface recombination of photogenerated $e-h$ pairs in the device.

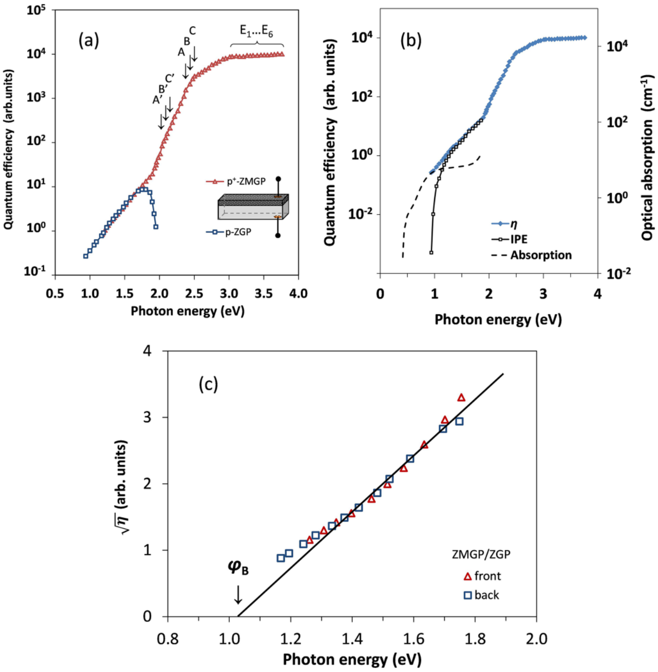

FIG. 14. (a) Quantum efficiency of ZMGP/ZGP heterojunction. (a) Spectra under front and back illuminations. Arrows denote minimum optical transitions in ZGP (pseudodirect and direct). The E$_1$ − E$_6$ interval corresponds to deep optical transitions. (b) Quantum efficiency η and internal photoemission (IPE) spectra of ZMGP/ZGP heterojunction in comparison with the optical absorption spectrum at deep levels of ZGP crystal. (c) Fowler photoemission of holes in the Schottky half-metal (HM) barrier of ZMGP/ZGP at room temperature.

The quantum efficiency is described by the equation [123]:

$$\eta = \frac{AJ_{\text{tot}}/q}{P_{\text{opt}}/\hbar\omega} = (1-R)\left[1 - \frac{\exp(-\alpha W_D)}{1+\alpha L_p}\right], \quad (10)$$

where W_{D} is the depletion-region width, $L_p = \sqrt{D_p\tau_p}$ the diffusion length of holes, D_p the diffusion coefficient for holes, and τ_p the lifetime of excess carriers.

Within the depletion region, the internal quantum efficiency $\eta_i(\hbar\omega) = 100\%$ has been assumed. In Eq. (10), $\eta(\hbar\omega)$ is reduced from unity due to the optical refection R and absorption α outside the depletion region $(W_{\text{D}} + L_p)$. The heterojunction illuminated from the backside shows a decrease in quantum efficiency at $\hbar\omega > 1.8$ eV, Fig. 14(a). The spectral decline corresponds to the onset of pseudodirect optical transitions in the ZGP substrate, accounting for the tails of the density of states in the conduction and valence bands.

The similarity of quantum efficiencies at low energies 1.0–1.75 eV for both front and back illuminations indicates that photoexcitation, charge carrier separation, and transport perform in the same way, regardless of light incidence, i.e., in the depletion region. The range $\hbar\omega < E_g$ is commonly characterized as IPE in heterojunctions and Schottky barriers [100,123]. For the ZMGP/ZGP heterojunction, these photon energies are below $\text{A}' = 1.99$ eV but above the energies of transitions through deep levels in the substrate [1], so the effect on IPE is minimal.

Figure 14(b) compares the optical (α), photonic (η), and IPA spectra of the ZGP crystal and ZMGP/ZGP heterojunction. The IPE curve is derived from the η spectrum under front illumination and is consistent with the reduced η of the Schottky barrier under back illumination. The spectrum at low energies is featured by IR optical absorption with a dropping signal at ~0.5 eV and a flat portion in the interval 1.0–1.8 eV. It is important to note that the photoemission of holes from the HMFM layer into the FM SC occurs in the same interval where the optical absorption is essentially flat; no absorption peaks associated with impurities or point defects were observed. At energies <1.0 eV, both photoemission and optical absorption diminish, and optical transitions through deep levels in ZPG become crucial. Thus, IPE in the range of 1.0–1.75 eV can be consistently described by the Fowler model with a quadratic dependence analogous to Schottky barriers with thin metallic layers [124,128,129].

Theoretical models developed for hole photoemission in metal/SC and SC/SC contacts [129–131] lead to the same expression $\eta \propto (\hbar\omega - \varphi_B)^2$ and are well confirmed experimentally on the $p^+ - p$ heterojunction under study. Figure 14(c) shows a plot of the square root of the quantum efficiency in the IPE range for holes photoemitted from HM to SC. The linear part of the spectral curve fits into a straight line with a cutoff, which in accordance with the Fowler model defines the barrier height $\varphi_B = 1.02$ eV. This height compares well with the pure metal barrier heights reported for III-V and II-IV-V_2 compound SCs with close band gaps [107,123,124]. The value $\varphi_B = 1.02$ eV for ZMGP/ZGP is close to that determined above from the *I-V* characteristic in the dark using the Richardson constant $A^{**} = 120\ \text{A/cm}^2\,\text{K}^2$ and the effective mass for HMs, which almost equals the mass of free charge carriers [126].

We expect that spin-polarized holes injected from FMHM into FM DMS do not suffer much attenuation of spin polarization as it happens for the direct injection into nonmagnetic SC. There are different mechanisms reducing the spin polarization: spin accumulation accompanied by backflow to a FM contact [132], intense spin-flip scattering [133], and the so-called conductance mismatch problem [134,135]. However, the latter problem can be overcome for HM/SC contact, and effective spin injection is possible [136]. The travel distance of spin-polarized holes is expected to be longer in the pair of two relative FM materials. In the ZMGP/ZGP heterojunction the magnetic order is kept at long distances, at least >1 μm determined by the Mn diffusion length. Additionally, spin polarization (P_n) can be enhanced for injected spin-polarized carriers (electrons) in materials with a high-to-low doping concentration profile [137,138]. In other words, the spin-diffusion length can dramatically increase due to the built-in positive electric field gradient that exists in the buffer layer ZGP:Mn.

IV. DISCUSSION

Mn-bound magnetic chains and nanoclusters were found in endotaxial ZMGP films, the arrangement of which is explained by the tetrahedron model. The tetrahedra are embedded in the crystal matrix without visible disturbance of the chalcopyrite structure. XRD analysis confirmed that the effect of lattice stress is small and negligible. We also found no evidence of phase segregation in the grown endotaxial films. It is important to note that MnP phase segregation can occur at elevated Mn concentrations in other chalcopyrite materials such as $CdSnP_2$ [139] or in strongly inhomogeneous materials [86,87]. As for the various compounds II-IV-V_2, some of them, e.g., $CdSnP_2$, decompose at high temperatures incongruently, while others, e.g., $ZnGeP_2$, melt congruently. Thus, similar solid-phase chemical reactions in different II-IV-V_2 ternary compounds lead to different products. The incorporation of manganese in $ZnGeP_2$ (001) is close to that in the binary analog GaP (001), where MnP nanoclusters have been observed [140–146]. Unlike compounds III-V, ternary compounds II-IV-V_2 readily accept any Mn concentration from 0 to 100% and easily achieve RTFM. This crystal-chemical advantage makes the endotaxial ZMGP/ZGP heterojunctions and the epitaxial MGP/GaAs and MGP/InP heterojunctions efficient diamondlike FM systems.

The ideal epitaxial growth on Si and Ge for other RT FMHM materials with diamondlike structure is still questionable. For example, in Heusler compounds, their cubic crystal lattice is structurally different from tetrahedrally coordinated GaAs, Si, and Ge materials and hence exhibits instability at the interface with them. Currently, several crystalline analogs in the diamond-sphalerite-chalcopyrite series appear more attractive for the growth of chemically and mechanically stable materials. The row Ge-GaP-$ZnGeP_2 - MnGeP_2$ has related crystal structures due to a similar Bravais lattice and close lattice constants. The binary GaP and the ordered ternary $In_{0.5}Ga_{0.5}P$ compounds are the closest to ZGP by structural, electronic, and mechanical properties. In the case of ZMGP/ZGP:Mn, endotaxial growth appears to be quite productive due to the convenient technology, the same diamondlike crystal structure, and the FM of both components.

In addition, the effect of crystal strain in epitaxial films can transform the material from insulator to metal [147], or the presence of crystallographic defects can shift the Fermi level and change the spin polarization at the Fermi level [148]. Variations in the lattice perfection of chalcopyrite lead to local optical anisotropy [1], spin-orbit and crystal field splittings [107], and changes in the Curie temperature in RTFM chalcopyrites [10,18,23,24,27,34]. Although the embedded $^{\mathrm{P}}_{\mathrm{P}}\!> \mathrm{Mn} <^{\mathrm{P}}_{\mathrm{P}}$ tetrahedral nanoclusters do not adversely affect the host crystal matrix, an increase in [Mn] leads to a DMS-to-HM transition, which is thought to be controlled by the percolation threshold [149,150]. Since the distribution of nanoclusters in the chalcopyrite matrix is considered diffusive, this issue can be addressed by percolation theory [151].

V. CONCLUSIONS

The Mn-rich ZMGP solid-state layer has been comprehensively investigated by several experimental methods, and the main essential attributes of HM—the properties of a SC and simultaneously a metal—have been demonstrated in the same substance. We found that the material is concurrently characterized by a nonzero energy gap $E_g = 0.099$ eV (SC), a sharp fundamental absorption edge typical of direct transitions (SC with parabolic bands), optical absorption in the fundamental band $\alpha > 2\times10^5$ cm^{-1} (SC), optical reflection with a plasma minimum (heavily doped SC), crystal structure (diamondlike SC), temperature dependence and absolute value of electrical resistivity (metal), dark current transport across the Schottky barrier (metal layer), and IPE of holes from the ZMGP layer into ZGP SC (metal layer). Based on a summary of optical, electrical, structural, and photoemission properties and relying on existing experimental data [31,39], we conclude that ZMGP is a HM at RT. This experimental evidence is supported by various theories of the HM state in Mn-doped chalcopyrites [18–22,25,28–30].

Mn-doped ZMGP layers have been successfully grown on ZGP (001) single crystals to incorporate the FM effect into a nonlinear optical medium and to achieve the hole photoemission at RT. The crystal structure of Mn-rich and poor layers contains magnetic chains and nanoclusters embedded in the chalcopyrite matrix without lattice deformation. The Mn-rich ZMGP film was proved to be a p-type conductivity HM at RT with a crystal structure of chalcopyrite and lattice constants close to ZGP crystal. The endotaxially grown layer forms a nearly perfect heterojunction with a robust diamondlike structure capable of withstanding strong light fluences.

The RTFM ZMGP can gain advantage in spintronics built exclusively on tetrahedral SCs such as Si, Ge, GaAs, and GaInP. Lattice matching in ZMGP/ZGP may allow overcoming the fundamental obstacle for electrical spin injection from a FM metal into a diffused SC [134,135], removal of a tunnel barrier, and reduction of spin-flip scattering in the $p^+ - p$ structure [133]. Magnetic technologies can also be conveniently combined in laser-based optical devices for mid-IR energy conversion by simply docking diamondlike FM films with the host chalcopyrite crystal. Finally, the diamondlike heterojunction with spin-polarized holes could be a useful FM model for HM spin emitters, oscillators, and potentially development of magnetically controlled nonlinear optical laser devices in the mid-IR range.

ACKNOWLEDGMENTS

Authors appreciate the support by Grant-in-Aid for Scientific Research in Japan from MEXT (Category No. 13305003) “Characterization of chalcopyrite-type room-temperature ferromagnetic semiconductors”. G.M. is grateful to Prof. Laurens W. Molenkamp (Würzburg University), Prof. Georg Schmidt (Martin-Luther-Universität Halle-Wittenberg), and Prof. Axel Hoffmann (Technical University, Berlin) for visiting professor grants that provided access to equipment and assistance with measurements, particularly Auger electron spectroscopy and HRXRD, for the DFG (Deutsche Forschungsgemeinschaft) project on “d-metal impurities in II-VI and II-IV-V$_2$ semiconductors.”

[1] G. Medvedkin, Optical dichroism in ZnGeP$_2$ crystals at deep levels, J. Opt. Soc. Am. B **39**, 851 (2022).

[2] P. G. Schunemann, K. T. Zawilski, L. A. Pomeranz, D. J. Creeden, and P. A. Budni, Advances in nonlinear optical crystals for mid-infrared coherent sources, J. Opt. Soc. Am. B **33**, D36 (2016).

[3] K. T. Zawilski, S. D. Setzler, P. G. Schunemann, and T. M. Pollak, Increasing the laser-induced damage threshold of single-crystal ZnGeP$_2$, J. Opt. Soc. Am. B **23**, 2310 (2006).

[4] N. Yudin, O. Antipov, I. Eranov, A. Gribenyukov, G. Verozubova, M. Zinoviev, S. Podzvalov, E. Slyunko, V. Voevodin, A. Zav’jalov *et al.*, Laser-induced damage threshold of single crystal ZnGeP$_2$ at 2.1 μm: The effect of crystal lattice quality at various pulse widths and repetition rates, Crystals **12**, 652 (2022).

[5] N. N. Yudin, O. L. Antipov, A. I. Gribenyukov, I. D. Eranov, S. N. Podzyvalov, M. M. Zinoviev, L. A. Voronin, E. V. Zhuravleva, and M. P. Zykova, Effect of postgrowth processing technology and laser radiation parameters at wavelengths of 2091 and 1064 nm on the laser-induced damage threshold in ZnGeP$_2$ single crystal, Quantum Electron. **51**, 306 (2021).

[6] G. Liu, S. Mi, K. Yang, D. Wei, J. Li, B. Yao, C. Yang, T. Dai, X. Duan, L. Tian *et al.*, 161 W middle infrared ZnGeP$_2$ MOPA system pumped by 300 W-class Ho:YAG MOPA system, Opt. Lett. **46**, 82 (2021).

[7] V. G. Dmitriev, G. G. Gurzadyan, and D. N. Nikogosyan, *Handbook of Nonlinear Optical Crystals*, 3rd rev. ed. (Springer, Berlin, 1999).

[8] R. L. Sutherland, *Handbook of Nonlinear Optics*, 2nd ed. (Dekker, New York, 2003), Chap. 3.

[9] K. Vodopyanov, Pulsed mid-IR optical parametric oscillators, in *Solid State Mid-Infrared Laser Sources* (Springer, Berlin, 2003), Chap. 4.

[10] G. A. Medvedkin, T. Ishibashi, T. Nishi, K. Hayata, Y. Hasegawa, and K. Sato, Room temperature ferromagnetism in novel diluted magnetic semiconductor Cd$_{1-x}$Mn$_x$GeP$_2$, Jpn. J. Appl. Phys. **39**, L949 (2000).

[11] G. A. Medvedkin, T. Ishibashi, T. Nishi, and K. Sato, New magnetic semiconductor Cd$_{1-x}$Mn$_x$GeP$_2$, Semiconductors **35**, 291 (2001).

[12] K. Sato, G. A. Medvedkin, T. Nishi, Y. Hasegawa, R. Misawa, K. Hirose, and T. Ishibashi, Ferromagnetic phenomenon revealed in the chalcopyrite semiconductor CdGeP$_2$:Mn, J. Appl. Phys. **89**, 7027 (2001).

[13] G. A. Medvedkin, K. Hirose, T. Ishibashi, T. Nishi, V. G. Voevodin, and K. Sato, New magnetic materials in ZnGeP$_2$ − Mn chalcopyrite system, J. Cryst. Growth **236**, 609 (2002).

[14] K. Sato, G. A. Medvedkin, and T. Ishibashi, Room temperature ferromagnetism in novel magnetic semiconductors based on II-IV-V$_2$ chalcopyrite compounds, J. Cryst. Growth **237**, 1363 (2002).

[15] K. Sato, G. A. Medvedkin, and T. Ishibashi, Room temperature ferro magnetic semiconductor and its fabrication, Japan Patent Application No. 2000 261367 (7 July 2000).

[16] K. Sato, G. A. Medvedkin, and T. Ishibashi, Magnetic semiconductor material and method for preparation thereof, World Patent WO 02/19352 A1 (3 July 2002).

[17] K. Sato, G. A. Medvedkin, and T. Ishibashi, Magnetic semiconductor material and method for preparation thereof, U.S. Patent 7102171 (5 September 2006).

[18] S. C. Erwin and I. Zutić, Tailoring ferromagnetic chalcopyrites, Nat. Mater. **3**, 410 (2004).

[19] S. Picozzi, Engineering ferromagnetism, Nat. Mater. **3**, 349 (2004).

[20] P. Mahadevan and A. Zunger, Room-temperature ferromagnetism in Mn-doped semiconducting $CdGeP_2$, Phys. Rev. Lett. **88**, 047205 (2002); **88**, 159904(E) (2002).

[21] T. Kamatani and H. Akai, Electronic structure and magnetism of novel diluted magnetic semiconductors $CdGeP_2$:Mn and $ZnGeP_2$:Mn, Phase Trans. **76**, 401 (2003).

[22] T. Kamatani and H. Akai, Magnetic properties of chalcopyrite-based diluted magnetic semiconductors, J. Supercond.: Incorp. Novel Magn. **16**, 95 (2003).

[23] S. Cho, S. Choi, G.-B. Cha, S. C. Hong, Y. Kim, Y.-J. Zhao, A. J. Freeman, J. B. Ketterson, B. J. Kim, Y. C. Kim *et al.*, Room-temperature ferromagnetism in $(Zn_{1-x}Mn_x)GeP_2$ semiconductors, Phys. Rev. Lett. **88**, 257203 (2002).

[24] S. Cho, S. Choi, G.-B. Cha, S. C. Hong, Y. Kim, A. J. Freeman, J. B. Ketterson, Y. Park, and H.-M. Park, Synthesis of new pure ferromagnetic semiconductors: $MnGeP_2$ and $MnGeAs_2$, Solid State Commun. **129**, 609 (2004).

[25] H. Yi and H. Park, Electronic structure and half-metallic ferromagnetism in $CdGe_{1-x}Mn_xP_2$ chalcopyrite semiconductor, J. Korean Phys. Soc. **45**, S530 (2004).

[26] Yu-Jun Zhao, W. T. Geng, A. J. Freeman, and T. Oguchi, Magnetism of chalcopyrite semiconductors: $Cd_{1-x}Mn_xGeP_2$, Phys. Rev. B **63**, 201202(R) (2001).

[27] S. Picozzi, A. Continenza, Y.-J. Zhao, W.-T. Geng, and A. J. Freeman, Structural, electronic and magnetic properties of chalcopyrite magnetic semiconductors: A first-principles study, J. Vac. Sci. Technol. A **20**, 2023 (2002).

[28] P. R. C. Kent and T. C. Schulthess, Ferromagnetism and carrier polarization of Mn-doped II-IV-V_2 chalcopyrites, AIP Conf. Proc. **772**, 1369 (2005).

[29] D. Vijayalakshmi and G. Kalpana, Electronic structure and magnetic properties of chalcopyrite type $ZnMX_2$ (M = Sc, V, Cr, Mn, Fe; X = P, As) compounds: An *ab initio* study, Phys. Status Solidi B **253**, 1576 (2016).

[30] B. Taychour, S. Zriouel, and L. B. Drissi, Half metallic ferromagnetic character in $ZnXP_2$ (X = Ge, Si) chalcopyrites doped with Mn, J. Supercond. Novel Magn. **32**, 1333 (2019).

[31] V. V. Popov and G. A. Medvedkin, Hole transport anomaly in high-T_C ferromagnet (Zn,Mn)GeP_2, Solid State Commun. **132**, 561 (2004).

[32] K. Sato, G. A. Medvedkin, K. Hayata, Y. Hasegawa, T. Nishi, R. Misawa, and T. Ishibashi, Magnetic and magneto-optical properties of a novel ferromagnetic semiconductor $CdGeP_2$:Mn, J. Magn. Soc. Japan **25**, 283 (2001).

[33] G. A. Medvedkin, P. G. Baranov, and S. I. Goloshchapov, Ferromagnetic properties of (Zn,Mn,Ge)P_2 layers on diamagnetic $ZnGeP_2$ single crystal substrates, J. Phys. Chem. Solids **64**, 1691 (2003).

[34] G. A. Medvedkin and V. G. Voevodin, Magnetic and optical phenomena in nonlinear optical crystals $ZnGeP_2$ and $CdGeP_2$, J. Opt. Soc. Am. B **22**, 1884 (2005).

[35] P. G. Baranov, S. I. Goloshchapov, G. A. Medvedkin, T. Ishibashi, and K. Sato, Magnetic resonance in $ZnGeP_2$ and (Zn,Mn)GeP_2, J. Supercond.: Incorp. Novel Magn. **16**, 131 (2003).

[36] P. G. Baranov, S. I. Goloshchapov, G. A. Medvedkin, and V. G. Voevodin, Detection of magnetic resonance signals with anomalous dispersion and two types of isolated manganese centers in the chalcopyrite crystal (Zn,Mn)GeP_2, JETP Lett. **77**, 582 (2003).

[37] P. G. Baranov, S. I. Goloshchapov, G. A. Medvedkin, V. G. Voevodin, S. B. Orlinskii, and J. Schmidt, Giant electron spin echo of ferromagnetic ordered manganese nanoclusters in (Zn,Mn)GeP_2 crystals, in *Proceeding of the 12th International Symposium Nanostructures: Physics and Technology* (Ioffe Institute, St. Petersburg, 2004), pp. 28–29.

[38] G. A. Medvedkin, V. V. Popov, S. I. Goloshchapov, P. G. Baranov, H. Blok, S. B. Orlinskii, and J. Schmidt, Study of magnetic clusters in the system ferromagnetic-nonmagnetic semiconductors (Zn,Mn)$GeP_2/ZnGeP_2$ by means of hole transport and magnetic resonance, in *Proceeding of the 13th International Symposium Nanostructures: Physics and Technology* (Ioffe Institute, St. Petersburg, 2005), pp. 149–150.

[39] Y. Ishida, D. D. Sarma, K. Okazaki, J. Okabayashi, J. I. Hwang, H. Ott, A. Fujimori, G. A. Medvedkin, T. Ishibashi, and K. Sato, *In situ* photoemission study of the room temperature ferromagnet $ZnGeP_2$:Mn, Phys. Rev. Lett. **91**, 107202 (2003).

[40] J.-H. Park, E. Vescovo, H.-J. Kim, C. Kwon, R. Ramesh, and T. Venkatesan, Direct evidence for a half-metallic ferromagnet, Nature (London) **392**, 794 (1998).

[41] Z. Sun, Q. Wang, J. F. Douglas, H. Lin, S. Sahrakorpi, B. Barbiellini, R. S. Markiewicz, A. Bansil, A. V. Fedorov, E. Rotenberg *et al.*, Minority-spin t_{2g} states and the degree of spin polarization in ferromagnetic metallic $La_{2-2x}Sr_{1+2x}Mn_2O_7$ ($x = 0.38$), Sci. Rep. **3**, 3167 (2013).

[42] X. L. Wang, Proposal for a new class of materials. spin gapless semiconductors, Phys. Rev. Lett. **100**, 156404 (2008).

[43] S. Ouardi, G. H. Fecher, C. Felser, and J. Kubler, Realization of spin gapless semiconductors: The Heusler compound Mn_2CoAl, Phys. Rev. Lett. **110**, 100401 (2013).

[44] Z. Yue, Z. Li, L. Sang, and X. Wang, Spin-gapless semiconductors, Small **16**, 1905155 (2020).

[45] D. Rani, L. Bainsla, A. Alam, and K. G. Suresh, Spin-gapless semiconductors: Fundamental and applied aspects, J. Appl. Phys. **128**, 220902 (2020).

[46] E. Sasioglu, T. Aull, D. Kutschabsky, S. Blügel, and I. Mertig, Half-metal–spin-gapless-semiconductor junctions as a route to the ideal diode, Phys. Rev. Appl. **14**, 014082 (2020).

[47] X. Wang, Z. Chen, G. Zhang, H. Yuan, H. Chen, and X. L. Wang, Spin-gapless semiconductors for future spintronics and electronics, Phys. Rep. **888**, 1 (2020).

[48] G. A. Medvedkin, Engineering of ternary ferromagnetic semiconductors in heterojunctions, J. Supercond.: Novel Magn. **16**, 135 (2003).

[49] K. Sato, T. Ishibashi, K. Minami, H. Yuasa, J. Jogo, T. Nagatsuka, A. Mizusawa, Y. Kangawa, and A. Koukitu, MBE growth of a novel chalcopyrite-type ternary compound $MnGeP_2$, J. Phys. Chem. Solids **66**, 2030 (2005).

[50] K. Minami, J. Jogo, V. Smirnov, H. Yuasa, T. Nagatsuka, T. Ishibashi, Y. Morishita, Y. Matsuo, Y. Kanagawa, A. Koukitu *et al.*, Growth of $MnGeP_2$ thin films by molecular beam epitaxy, Jap. J. Appl. Phys. **44**, L265 (2005).

[51] K. Minami, V. M. Smirnov, H. Yuasa, J. Jogo, T. Nagatsuka, T. Ishibashi, and K. Sato, MBE growth of $MnGeP_2$ thin films, J. Cryst. Growth **275**, e2225 (2005).

[52] J. Choi, Y.-H. Hwang, J. H. Kim, S. Cho, and C.-C. Tsai, MBE growth and transport properties of $MnGeP_2$ under various P pressure, J. Korean Phys. Soc. **55**, 2677 (2009).

[53] Y. Cui, W. Mu, J. Lee, J. Song, Y. Kim, and J. B. Ketterson, and S. Cho, Magnetic and transport properties of $MnGeP_2$ films grown on GaAs(001) by molecular beam epitaxy, J. Appl. Phys. **97**, 10M518 (2005).

[54] J. Choi, Y. H. Hwang, S. Choi, S. C. Hong, and S. Cho, Magneto-transport properties of $MnGeP_2$ ferromagnetic semiconductor, J. Magn. Magn. Mat. **310**, 2117 (2007).

[55] X. Jiang and W. R. L. Lambrecht, The importance of the self-interaction correction for Jahn–Teller distortion of the zinc vacancy in $ZnGeP_2$, Solid State Commun. **149**, 685 (2009).

[56] X. Jiang and W. R. L. Lambrecht, Jahn-Teller distortion of the zinc vacancy in $ZnGeP_2$, Chin. Phys. Lett. **25**, 1075 (2008).

[57] X. Jiang, M. S. Miao, and W. R. L. Lambrecht, Theoretical study of the phosphorus vacancy in $ZnGeP_2$, Phys. Rev. B **73**, 193203 (2006); Theoretical study of cation-related point defects in $ZnGeP_2$, **71**, 205212 (2005).

[58] S. Limpijumnong, W. R. L. Lambrecht, and B. Segall, Electronic structure of $ZnGeP_2$: A detailed study of the band structure near the fundamental gap and its associated parameters, Phys. Rev. B **60**, 8087 (1999).

[59] M. Huang, S.-S. Wang, Y.-N. Wu, and S. Chen, Defect physics of ternary semiconductor $ZnGeP_2$ with a high density of anion-cation antisites: A first-principles study, Phys. Rev. Appl. **15**, 024035 (2021).

[60] D. Naveh and L. Kronik, Spin-polarized electronic structure of Mn–IV–V_2 chalcopyrites, Phys. Status Solidi B **243**, 2159 (2006).

[61] *Concepts in Spin Electronics*, edited by S. Maekawa (Oxford University Press, New York, 2006).

[62] *Spin Physics in Semiconductors*, edited by M. I. Dyakonov (Springer, Berlin, 2008).

[63] *Spintronics*, edited by T. Dietl, D. D. Awschalom, M. Kaminska, and H. Ohno (Elsevier, Amsterdam, 2008).

[64] *Magnetic Heterostructures: Advances and Perspectives in Spinstructures and Spintransport*, edited by H. Zabel and S. D. Bader (Springer, Berlin, 2008).

[65] *Spintronics: Materials, Applications, and Devices*, edited by G. C. Lombardi and G. E. Bianchi (Nova Science, New York, 2009).

[66] *Spin Current*, edited by S. Maekawa, S. O. Valenzuela, E. Saitoh, and T. Kimura (Oxford University Press, Oxford, 2012).

[67] *Spintronics from Materials to Devices*, edited by C. Felser and G. H. Fecher (Springer, Dordrecht, 2013).

[68] *Spintronics for Next Generation Innovative Devices*, edited by E. Saitoh and K. Sato (John Wiley, Chichester, 2015).

[69] *Spintronics Handbook: Spin Transport and Magnetism*, 2nd ed., edited by E. Y. Tsymbal and I. Žutić (CRC Press, Boca Raton, 2019), Vol. 1–3.

[70] S. Olive-Mendez, A. Spiesser, L. A. Michez, V. Le Thanh, A. Glachant, J. Derrien, T. Devillers, A. Barski, and M. Jamet, Epitaxial growth of Mn_5Ge_3/Ge(111) heterostructures for spin injection, Thin Sol. Films **517**, 191 (2008).

[71] S. Fiechter, A. Kurzweil, H. Castleberry, and K. J. Bachmann, Composition of the equilibrium vapor phase over $ZnGeP_2$ and thermal stability, MRS Proc. **450**, 321 (1997).

[72] A. A. Vaipolin, E. O. Osmanov, and D. N. Tretyakov, Some aspects of the chemistry of diamond-like compounds of the type $A^2B^4C^5_2$, Inorg. Mater. **3**, 260 (1967).

[73] G. E. McGuire, *Auger Electron Spectroscopy Reference Manual. A Book of Standard Spectra for Identification and Interpretation of Auger Electron Spectroscopy Data* (Springer, New York, 1979).

[74] J. F. Watts and J. Wolstenholme, *An Introduction to Surface Analysis by XPS and AES* (Wiley, Chichester, 2003).

[75] J. M. Lannon, Jr. and C. D. Stinespring, Auger electron spectroscopy in analysis of surfaces, in *Encyclopedia of Analytical Chemistry*, edited by R. A. Myers (Wiley, Chichester, 2000), pp. 9033–9047.

[76] *Surface Analysis—The Principal Techniques*, 2nd ed., edited by J. C. Vickerman and I. S. Gilmore (Wiley, Chichester, 2009).

[77] B. L. Henke, E. M. Gullikson, and J. C. Davis, X-ray interactions: Photoabsorption, scattering, transmission, and reflection at $E = 50$–$30\,000$ eV, $Z = 1$–92, At. Data Nucl. Data Tables **54**, 181 (1993).

[78] N. P. Grazhdankina, A. M. Burkhanov, and Y. S. Bersenev, The effect of hydrostatic pressure on the Curie temperature of manganese monophosphide, Sov. Phys. JETP **28**, 1141 (1969).

[79] The Materials Project, MnP (mp-2662, mp-1009135), database version v2022.10.28, https://next-gen.materialsproject.org.

[80] G. F. Harrington and J. Santiso, Back-to-basics tutorial: X-ray diffraction of thin films, J. Electroceram. **47**, 141 (2021).

[81] PDF card #00-050-1210, The International Centre for Diffraction Data (2022).

[82] PDF card #01-073-0398, The International Centre for Diffraction Data (2022).

[83] L. Hong-Gang, W. Xiao-Xuan, and Z. Wen-Chen, Zero-field splittings and local tilting angles $\tau_{Mn^{2+}}$ for Mn^{2+} in $ZnGeP_2$ and $CdGeP_2$ crystals, Spectrochim. Acta Part A **71**, 417 (2008).

[84] T. Hwang, J. H. Shim, and S. Lee, Observation of MnP magnetic clusters in room-temperature ferromagnetic semiconductor $Zn_{1-x}Mn_xGeP_2$ using nuclear magnetic resonance, Appl. Phys. Lett. **83**, 1809 (2003).

[85] P. W. Mengyan, R. L. Lichti, Y. G. Celebi, B. B. Baker, B. R. Carroll, E. Catak, K. T. Zawilski, and P. G. Schunemann, Magnetic fields and fluctuations in weakly Mn doped $ZnGeP_2$, AIP Conf. Proc. **1583**, 190 (2014).

[86] L. Kilanski, S. Lewińska, A. Khaliq, R. Minikaev, A. Reszka, A. Ślawska-Waniewska, B. J. Kowalski, T. R. Arslanov, and S. F. Marenkin, From ferromagnetic to helical order with a discussion of the low-temperature antiferromagnetism in composite $Cd_{1-x}Mn_xGeP_2 +$ MnP semiconductors, Phys. Rev. B **104**, 184430 (2021).

[87] T. R. Arslanov, A. Yu. Mollaev, I. K. Kamilov, R. K. Arslanov, L. Kilanski, R. Minikaev, A. Reszka, S. Lopez-Moreno, A. H. Romero, M. Ramzan *et al.*, Pressure control of magnetic clusters in strongly inhomogeneous ferromagnetic chalcopyrites, Sci. Rep. **5**, 7720 (2015).

[88] A. Continenza, S. Picozzi, W. T. Geng, and A. J. Freeman, Coordination and chemical effects on the structural, electronic,

and magnetic properties in Mn pnictides, Phys. Rev. B **64**, 085204 (2001).

[89] M. K. Horton, J. H. Montoya, M. Liu, and K. A. Persson, High-throughput prediction of the ground-state collinear magnetic order of inorganic materials using density functional theory, npj Comput. Mater. **5**, 64 (2019).

[90] Y.-J. Zhao, P. Mahadevan, and A. Zunger, Practical rules for orbital-controlled ferromagnetism of 3*d* impurities in semiconductors, J. Appl. Phys. **98**, 113901 (2005).

[91] L. E. Halliburton, G. J. Edwards, M. P. Scripsick, M. H. Rakowsky, P. G. Schunemann, and T. M. Pollak, Electron-nuclear double resonance of the zinc vacancy in $ZnGeP_2$, Appl. Phys. Lett. **66**, 2670 (1995).

[92] K. T. Stevens, S. D. Setzler, L. E. Halliburton, N. C. Fernelius, P. G. Schunemann, and T. M. Pollak, Electron-nuclear double resonance study of the zinc vacancy in zinc germanium phosphide ($ZnGeP_2$), Proced. MRS **484**, 549 (1998).

[93] S. D. Setzler, N. C. Giles, L. E. Halliburton, P. G. Schunemann, and T. M. Pollak, Electron paramagnetic resonance of a cation antisite defect in $ZnGeP_2$, Appl. Phys. Lett. **74**, 1218 (1999).

[94] T. D. Gustafson, N. C. Giles, P. G. Schunemann, K. T. Zawilski, K. L. Averett, J. E. Slagle, and L. E. Halliburton, Intrinsic point defects (vacancies and antisites) in $CdGeP_2$ crystals, J. Appl. Phys. **133**, 245703 (2023).

[95] M. Fox, *Optical Properties of Solids*, 2nd ed. (Oxford University Press, New York, 2010), Chaps. 1 and 7.

[96] D.-H. Yang and X.-L. Cao, Effect of weak Mn doping on optical properties of $ZnGeP_2$ single crystal grown by vertical gradient freezing method, Mater. Res. Express **7**, 105905 (2020).

[97] C. V. de Alvarez, M. L. Cohen, S. E. Kohn, Y. Petroff, and Y. R. Shen, Calculated and measured reflectivity of $ZnGeP_2$, Phys. Rev. B **10**, 5175 (1974).

[98] J. C. Rife, R. N. Dexter, P. M. Bridenbaugh, and B. W. Veal, Optical properties of the chalcopyrite semiconductors $ZnGeP_2$, $ZnGeAs_2$, $CuGaS_2$, $CuAlS_2$, $CuInSe_2$, and $AgInSe_2$, Phys. Rev. B **16**, 4491 (1977).

[99] A. Kheirandish, N. S. Javan, and H. Mohammadzadeh, Modified Drude model for small gold nanoparticles surface plasmon resonance based on the role of classical confinement, Sci. Rep. **10**, 6517 (2020).

[100] T. S. Moss, G. J. Burrell, and B. Ellis, *Semiconductor Opto-Electronics* (Butterworth, London, 1973).

[101] L. L. Chase, Optical properties of CrO_2 and MoO_2 from 0.1 to 6 eV, Phys. Rev. B **10**, 2226 (1974).

[102] E. J. Singley, C. P. Weber, D. N. Basov, A. Barry, and J. M. D. Coey, Charge dynamics in the half-metallic ferromagnet CrO_2, Phys. Rev. B **60**, 4126 (1999).

[103] E. I. Shreder, A. A. Makhnev, A. V. Lukoyanov, and K. G. Suresh, Optical properties and the electronic structure of Co_2TiGe and Co_2TiSn Heusler alloys, Phys. Metals. Metallogr. **118**, 965 (2017).

[104] M. M. Kirillov, A. A. Makhnev, E. I. Shreder, V. P. Dyakina, and N. B. Gorina, Interband optical absorption and plasma effects in half-metallic XMnY ferromagnets, Phys. Stat. Solidi B **187**, 231 (1995).

[105] G. A. Medvedkin, Y. V. Rud, and M. A. Tairov, Direct observation of valence-band crystal-field splitting in $CdSiAs_2$, Solid State Commun. **71**, 307 (1989).

[106] G. A. Medvedkin, Yu. V. Rud, and M. A. Tairov, Optical dichroism of $CdSnP_2$ crystals near the fundamental absorption edge, Fiz. Tverd. Tela **31**, 108 (1989) [Sov. Phys. Solid State **31**, 606 (1989)].

[107] G. A. Medvedkin, Y. V. Rud, and M. A. Tairov, Photoelectric anisotropy of II-IV-V_2 ternary semiconductors, Phys. Status Solidi A **115**, 11 (1989).

[108] G. Medvedkin, Radiative transitions in undoped and Mn-doped $CdGeP_2$ crystals, Phys. Rev. B **109**, 205206 (2024).

[109] G. A. Medvedkin, V. M. Smirnov, T. Ishibashi, and K. Sato, Photoluminescence of $CdGeP_2$ and (Cd,Mn)GeP_2, J. Phys. Chem. Solids **66**, 2015 (2005).

[110] P. D. Desai, H. M. James, and C. Y. Ho, Electrical resistivity of aluminium and manganese, J. Phys. Chem. Ref. Data **13**, 1131 (1984).

[111] R. V. Bellau and B. R. Coles, Magnetic Brillouin zone effects in the electrical resistivity of manganese and some manganese alloys, Proc. Phys. Soc. **82**, 121 (1963).

[112] A. Takase and T. Kasuya, Temperature dependences of electrical resistivity in MnP, J. Phys. Soc. Jap. **48**, 430 (1980).

[113] P. Zheng, Y. J. Xu, W. Wu, G. Xu, J. L. Lv, F. K. Lin, P. Wang, Y.-f. Yang, and J. L. Luo, Orbital-dependent charge dynamics in MnP revealed by optical study, Sci. Rep. **7**, 14178 (2017).

[114] S. P. Lewis, P. B. Allen, and T. Sasaki, Band structure and transport properties of CrO_2, Phys. Rev. B **55**, 10253 (1997).

[115] S. M. Watts, S. Wirth, S. von Molnár, A. Barry, and J. M. D. Coey, Evidence for two-band magnetotransport in half-metallic chromium dioxide, Phys. Rev. B **61**, 9621 (2000).

[116] J. Choi, S. Choi, M. H. Sohn, H. Park, Y. Park, H.-M. Park, S. C. Hong, and S. Cho, Epitaxial MnP thin films: Epitaxial growth, magnetic and electrical properties, J. Magn. Magn. Mater. **304**, e112 (2006).

[117] S. J. Ahmed, C. Boyer, and M. Niewczas, Magnetic and structural properties of Co_2MnSi based Heusler compound, J. Alloys Comp. **781**, 216 (2019).

[118] L. Ritchie, G. Xiao, Y. Ji, T. Y. Chen, C. L. Chien, M. Zhang, J. Chen, Z. Liu, G. Wu, and X. X. Zhang, Magnetic, structural, and transport properties of the Heusler alloys Co_2MnSi and NiMnSb, Phys. Rev. B **68**, 104430 (2003).

[119] S. Picozzi and A. J. Freeman, Polarization reduction in half-metallic Heusler alloys: The effect of point defects and interfaces with semiconductors, J. Phys.: Condens. Matter **19**, 315215 (2007).

[120] K. Elphick, W. Frost, M. Samiepour, T. Kubota, K. Takanashi, H. Sukegawa, S. Mitani, and A. Hirohata, Heusler alloys for spintronic devices: Review on recent development and future perspectives, Sci. Technol. Adv. Mater. **22**, 235 (2021).

[121] M. Jourdan, J. Minar, J. Braun, A. Kronenberg, S. Chadov, B. Balke, A. Gloskovskii, M. Kolbe, H. J. Elmers, G. Schonhense *et al.*, Direct observation of half-metallicity in the Heusler compound Co_2MnSi, Nat. Commun. **5**, 3974 (2014).

[122] S. K. Cheung and N. W. Cheung, Extraction of Schottky diode parameters from forward current-voltage characteristics, Appl. Phys. Lett. **49**, 85 (1986).

[123] S. M. Sze and K. K. Ng, *Physics of Semiconductor Devices*, 3rd ed. (Wiley, Hoboken, 2007).

[124] E. H. Rhoderick and R. H. Williams, *Metal-Semiconductor Contacts*, 2nd ed. (Oxford University Press, Oxford, 1988).

[125] K. Somogyi and I. Bertoti, Some electrical properties of $ZnGeP_2$ crystals, Jpn. J. Appl. Phys. **11**, 103 (1972).

[126] C. M. Fang, G. A. de Wijs, and R. A. de Groot, Spin-polarization in half-metals (invited), J. Appl. Phys. **91**, 8340 (2002).

[127] R. F. Schmitsdorf, T. U. Kampen, and W. Mönch, Explanation of the linear correlation between barrier heights and ideality factors of real metal-semiconductor contacts by laterally nonuniform Schottky barriers, J. Vac. Sci. Technol. B **15**, 1221 (1997).

[128] R. H. Fowler, The analysis of photoelectric sensitivity curves for clean metals at various temperatures, Phys. Rev. **38**, 45 (1931).

[129] R. J. Powell, Interface barrier energy determination from voltage dependence of photoinjected currents, J. Appl. Phys. **41**, 2424 (1970).

[130] J. S. Helman and F. Sánchez-Sinencio, Theory of internal photoemission, Phys. Rev. B **7**, 3702 (1973).

[131] C. Caroli, J. S. Helman, and F. Sánchez Sinencio, Internal photoemission of holes from a semiconductor into a semiconductor, Phys. Rev. B **11**, 980 (1975).

[132] R. Jansen, A. Spiesser, H. Saito, and S. Yuasa, Nonlinear spin transport in a rectifying ferromagnet/semiconductor Schottky contact, Phys. Rev. B **92**, 075304 (2015).

[133] J. D. Albrecht and D. L. Smith, Electron spin injection at a Schottky contact, Phys. Rev. B **66**, 113303 (2002); Spin-polarized electron transport at ferromagnet/semiconductor Schottky contacts, **68**, 035340 (2003).

[134] G. Schmidt, D. Ferrand, L. W. Molenkamp, A. T. Filip, and B. J. van Wees, Fundamental obstacle for electrical spin injection from a ferromagnetic metal into a diffusive semiconductor, Phys. Rev. B **62**, R4790(R) (2000).

[135] G. Schmidt, Concepts for spin injection into semiconductors—A review, J. Phys. D: Appl. Phys. **38**, R107 (2005).

[136] K. D. Belashchenko, J. K. Glasbrenner, and A. L. Wysocki, Spin injection from a half-metal at finite temperatures, Phys. Rev. B **86**, 224402 (2012).

[137] D. Csontos and S. E. Ulloa, Spin polarization control in semiconductors by electric-field gradients, Phys. Rev. B **74**, 155207 (2006).

[138] A. Hirohata, Y. B. Xu, C. M. Guertler, J. A. C. Bland, and S. N. Holmes, Spin-polarized electron transport in ferromagnet/semiconductor hybrid structures induced by photon excitation, Phys. Rev. B **63**, 104425 (2001).

[139] J. A. Aitken, G. M. Tsoi, L. E. Wenger, and S. L. Brock, Phase segregation of MnP in chalcopyrite dilute magnetic semiconductors: A cautionary tale, Chem. Mater. **19**, 5272 (2007).

[140] C. Lacroix, S. Lambert-Milot, P. Desjardins, R. A. Masut, and D. Menard, Surface induced magnetization reversal of MnP nanoclusters embedded in GaP, J. Appl. Phys. **119**, 103901 (2016).

[141] N. Nateghi, S. Lambert-Milot, D. Ménard, and R. A. Masut, Manganese phosphide thin films and nanorods grown on gallium phosphide and on glass substrates, J. Cryst. Growth **442**, 75 (2016).

[142] C. Lacroix, S. Lambert-Milot, P. Desjardins, R. A. Masut, and D. Menard, Magnetic anisotropy in GaP (001) epilayers containing MnP nanoclusters observed by angle dependent ferromagnetic resonance measurements, J. Appl. Phys. **103**, 07D531 (2008).

[143] C. Lacroix, S. Lambert-Milot, R. A. Masut, P. Desjardins, and D. Ménard, Ferromagnetic resonance measurements of GaP epilayers with embedded MnP nanoclusters grown on GaP(001), Phys. Rev. B **87**, 024412 (2013).

[144] A. de Andrés, A. Espinosa, C. Prieto, M. García-Hernández, R. Ramírez-Jiménez, S. Lambert-Milot, and R. A. Masut, MnP films and MnP nanocrystals embedded in GaP epilayers grown on GaP(001): Magnetic properties and local bonding structure, J. Appl. Phys. **109**, 113910 (2011).

[145] A. de Andrés, R. Ramírez-Jiménez, M. García-Hernández, S. Lambert-Milot, and R. A. Masut, Confinement effects on the low temperature magnetic structure of MnP nanocrystals, Appl. Phys. Lett. **99**, 182506 (2011).

[146] S. Lambert-Milot, C. Lacroix, D. Ménard, R. A. Masut, P. Desjardins, M. Garcia-Hernandez, and A. de Andres, Metal-organic vapor phase epitaxy of crystallographically oriented MnP magnetic nanoclusters embedded in GaP(001), J. Appl. Phys. **104**, 083501 (2008).

[147] D. Li, B. Zhu, D. Backes, L. S. I. Veiga, T.-L. Lee, H. Wang, Q. He, P. Roy, J. Zhang, J. Shi *et al.*, Manipulating the metal-to-insulator transition and magnetic properties in manganite thin films via epitaxial strain, Phys. Rev. B **105**, 165426 (2022).

[148] G. G. Baez Flores, I. A. Zhuravlev, and K. D. Belashchenko, Effects of intrinsic defects and alloying with Fe on the half-metallicity of Co_2MnSi, Phys. Rev. Mater. **4**, 024414 (2020).

[149] A. Kaminski and S. Das Sarma, Magnetic and transport percolation in diluted magnetic semiconductors, Phys. Rev. B **68**, 235210 (2003).

[150] N. Uchitomi, S. Hidaka, S. Saito, J. T. Asubar, and H. Toyota, Magnetic phase change in Mn-doped $ZnSnAs_2$ thin films depending on Mn concentration, J. Appl. Phys. **123**, 161566 (2018).

[151] B. I. Shklovskii and A. L. Efros, Electronic properties of doped semiconductors, *Percolation Theory* (Springer, Berlin, 1984), Chap. 5.